Mériaux CA, Mériaux AS, Schellart WP, Duarte JC, Duarte SS, Chen Z.
Mantle plumes in the vicinity of subduction zones.
***Earth and Planetary Science Letters* 2016, 454, 166-177**

Mantle plumes in the vicinity of subduction zones

C.A. Mériaux[a,c,*], A-S. Mériaux[b], W.P. Schellart[c,d], J.C. Duarte[e,c], S.S. Duarte[c], Z. Chen[c]

[a]*School of Physics and Astronomy, Monash University, Melbourne, Australia.*
[b]*School of Geography, Politics and Sociology, Newcastle University, UK.*
[c]*School of Earth, Atmosphere and Environment, Monash University, Melbourne, Australia.*
[d]*Faculty of Earth and Life Sciences, Vrije Universiteit Amsterdam, Amsterdam, Netherlands*
[e]*Instituto Dom Luiz, Universidade de Lisboa, 1749-016 Lisboa, Portugal.*

Abstract

We present three-dimensional deep-mantle laboratory models of a compositional plume within the vicinity of a buoyancy-driven subducting plate with a fixed trailing edge. We modelled front plumes (in the mantle wedge), rear plumes (beneath the subducting plate) and side plumes with slab/plume systems of buoyancy flux ratio spanning a range from 2 to 100 that overlaps the ratios in nature of 0.2-100. This study shows that 1) rising side and front plumes can be dragged over thousands of kilometres into the mantle wedge, 2) flattening of rear plumes in the trench-normal direction can be initiated 700 km away from the trench, and a plume material layer of lesser density and viscosity can ultimately almost entirely underlay a retreating slab after slab/plume impact, 3) while side and rear plumes are not tilted until they reach $\sim$ 600 km depth, front plumes can be tilted at increasing depths as their plume buoyancy is lessened, and rise at a slower rate when subjected

*Corresponding author
Email addresses: catherine.meriaux@monash.edu (C.A. Mériaux)

to a slab-induced downwelling, 4) rear plumes whose buoyancy flux is close to that of a slab, can retard subduction until the slab is 600 km long, and 5) slab-plume interaction can lead to a diversity of spatial plume material distributions into the mantle wedge. We discuss natural slab/plume systems of the Cascadia/Bowie-Cobb, and Nazca/San Felix-Juan Fernandez systems on the basis of our experiments and each geodynamic context and assess the influence of slab downwelling at depths for the starting plumes of Java, Coral Sea and East Solomon. Overall, this study shows how slab/plume interactions can result in a variety of geological, geophysical and geochemical signatures.

Key words:

subduction, mantle plume, analog modelling, mantle flow, slab rollback.

---

1. Introduction

In the theory of plate tectonics, subduction zones and mantle plumes (hotspots) are described as two distinctive elements of mantle convection. Subduction carries cool oceanic lithosphere downward and plumes carry hot mantle from the deep interior toward the surface (Schubert, 2001). Hotspots have preferentially been located near divergent plate boundaries, and excluded from regions near convergent plate boundaries (e.g. Weinstein and Olson, 1989). However today's observations based mostly on tomographic studies suggest the presence of plumes in the vicinity of subduction zones (e.g. Obrebski et al., 2010). Such spatial proximity could have important geodynamic implications such as flattening of subduction (Dalziel et al., 2000), plume deflection, widespread magmatism (Geist & Richards, 1993), rapid

switches in tectonic modes, modified crustal growth (Wyman et al., 2002) and the formation of mineral deposits such as gold (Wyman et al., 1999).

Proposed examples of modern slab/plume interaction include the Cascadia subduction zone and the Yellowstone hotspot (Murphy et al., 1998; Smith et al., 2009), the Tonga subduction zone and the Samoa hotspot (Smith et al., 2001), and the Kamchatka subduction zone segment and the Kamchatka plume (Gorbatov et al., 2001). In the last 60 Myr, 29% and 17% of the commonly recognised mantle plumes have been within 1000 km and 500 km, respectively, of a subduction zone (Fletcher and Wyman, 2015). In the more distant geologic past, proposed examples include the interaction of the South Greenland and central Scandinavia subduction zones with a plume located between Baltica and Greenland at $\sim$ 1284-1234 Ma (Söderlund et al., 2006), interaction of the retreating Gondwanan margin and the plume responsible for the Jurassic Karroo-Ferrar flood basalts (Dalziel et al., 2000), and the Mesoproterozoic plume-modified orogenesis in eastern Precambrian Australia (Betts et al., 2009).

Until recently, the different models that have been envisaged to explain the geological and geophysical observations have mostly been conceptual. For example, we know that mantle plumes can be deflected by mantle flow (Kerr and Mériaux, 2004) but the conditions under which a subducting plate captures a plume remain unknown. The influence of a mantle plume on a slab is not well known either. Such questions critically demand to be tested by dynamic models as they have clear importance in a number of geological environments.

Recently, Morishige et al. (2010) implemented two-dimensional numerical

simulations of a hot anomaly adjacent to a cold kinematically-driven downgoing slab to test the origin of a low velocity anomaly under the subducting Pacific plate. Similarly, Lee and Lim (2014) used a two-dimensional model of a cold kinematically-driven downgoing slab with a short-term temperature anomaly into the mantle wedge to assess slab melting, and the occurrence of the Abukuma adakite in northeastern Japan. Using three-dimensional numerical simulations, Betts et al. (2012, 2015) modelled the behaviour of subducting plates encoutering a plume head prescribed, either at the base of the subducting plate or at the base of the overriding plate, by a volume of lesser density and viscosity. These studies quantified the manner in which a plume head could modify trench and slab geometry. Besides those numerical investigations, a small number of laboratory models have been presented. Kincaid et al. (2013) and Druken et al. (2014) carried out experiments with a rigid and kinematically driven subducting plate in interaction with a thermal plume to model the bifurcation of the Yellowstone plume and the entrainment of the Samoan plume in the Lau basin, respectively. Mériaux et al. (2015a, 2015b) presented three-dimensional upper-mantle laboratory models of the Gibraltar subduction zone and Canary plume, and the Manila subduction zone and Hainan plume. These recent quantitative studies have been significant steps forward in the understanding of slab/plume interaction, but they were all case studies. Here we present the first generic study of such interaction, as the stage for more systematic studies to come given the complexity of the interaction.

In this paper, we report deep mantle laboratory analog experiments of a compositional plume within the vicinity of a buoyancy-driven slab with a

fixed trailing plate. We present a set of 21 experiments, in which we vary the slab/plume buoyancy flux ratio over a range of 2-100 overlapping that of nature, and the initial plume source relative to a fixed trailing-edge slab. Our experiments highlight the conditions under which the slab-induced poloidal and toroidal flows affect the plume dynamics and vice-versa. Natural cases of plumes in the vicinity of a subduction zone are finally discussed.

2. Analogue Modelling

We used a Perspex tank 1 m long, 0.62 m wide and 0.60 m deep that was filled with glucose syrup, a Newtonian fluid, up to H=0.45 m. A plate of thickness d=0.015 m, width W=0.20 m, and length L=0.50 or 0.60 m made of high-viscosity linear-viscous silicone (Wacker Silicone) mixed with fine iron powder was used to model an oceanic plate. The glucose syrup density was ρ_a = 1413 kg/m^3, and its viscosity μ_a varied within the range 74-119 Pa s due to temperature variations. The plate density of 1513 kg/m^3 was larger than that of the glucose by $\Delta\rho_s$=100 kg/m^3. The plate dynamic shear viscosity μ_s of 64,000 Pa s was substantially larger than the glucose syrup viscosity μ_a as the ratio $\gamma = \mu_s/\mu_a$ was within the range 538–865. The plate was fixed along its trailing edge to one of the lateral walls. Subduction of the plate was initiated by downward bending a length of its free edge l_{top} equivalent to 3 cm as measured from the top by an angle θ_0. Black neutrally buoyant spheres to be used as slab-induced flow tracers were spread at the top surface. A compositional plume was introduced at the base of the tank through a nozzle. The plume fluid was made of glucose syrup diluted with water resulting in a plume density less than that of the glucose syrup by

$\Delta\rho_p$=40 kg/m^3, and a viscosity $\mu_p = 5$ Pa s. The buoyant fluid was supplied by a pressure vessel and was dyed to make the plume clearly visible. In each experiment, we maintained a constant input volume flux Q. Figure 1 shows the laboratory setup and the different initial plume positions. Photos were taken every 10 seconds simultaneously from two sides, and from the top.

Lengths of the model were scaled so that 1 cm represents 50 km in nature. The time was scaled by the time a slab element takes to sink through the model depth H at the velocity scale $\hat{U} = \Delta\rho_s g d^2/\mu_a = \gamma\Delta\rho_s g d^2/\mu_s$, resulting in

$$\frac{t^{Nature}}{t^{Model}} = \frac{H^{Nature}}{\hat{U}^{Nature}} \times \frac{\hat{U}^{Model}}{H^{Model}} = \left(\frac{H^{Nature}}{H^{Model}}\right)\left(\frac{(\gamma\Delta\rho_s g d^2/\mu_s)^{Model}}{(\Delta\rho_s g d^2/\mu_a)^{Nature}}\right), \quad (1)$$

where g is the gravitational acceleration. Hence one second typically represents about 7 kyr, using a model γ, a mantle depth H and mantle viscosity μ_a of 640, 2000 km and 10^{20} Pa s, respectively. The presented models are deep mantle models and no stratification of the mantle is considered. We defined the slab buoyancy flux B_s by

$$B_s/g = \Delta\rho_s U W d, \quad (2)$$

where U is the slab steady sinking rate, while the plume buoyancy flux B_p is given by

$$B_p/g = \Delta\rho_p Q, \quad (3)$$

(see also Appendix S1). In experiments 4-21, as well as the plume relative position to the slab, we varied the buoyancy flux ratio B_s/B_p.

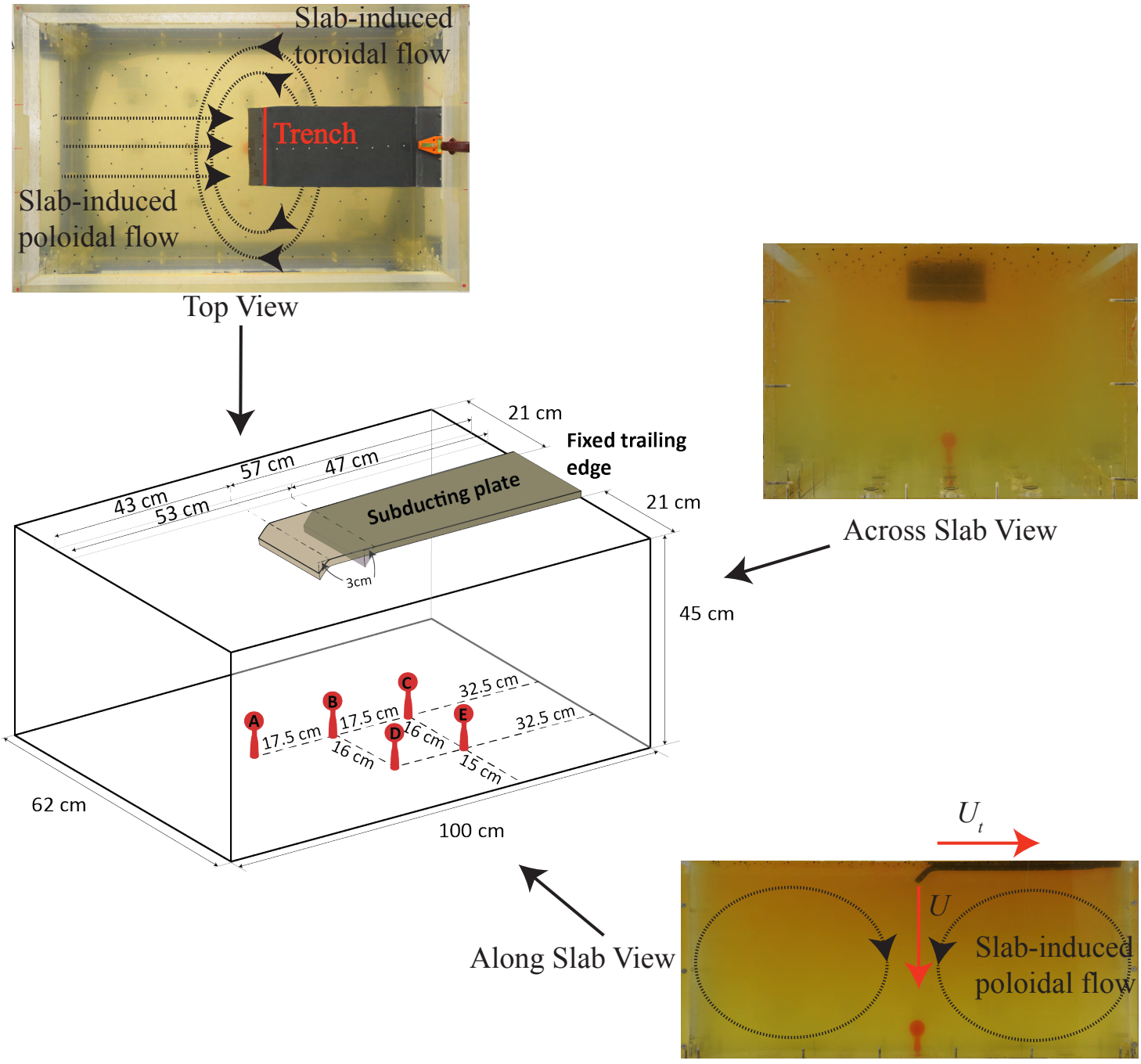

Figure 1: Experimental setting. The plume positions used for the experiments are shown and referred to in Table 1.

Experiments		W	d	L	γ	θ_0	S_0	U_0^*	U	U_{edge}	B_s/g	B_p/g	B_s/B_p
		(cm)	(cm)	(cm)		(degrees)		(cm/s)	(cm/s)	(cm/s)	(kg/s)	(kg/s)	
Errors					10%	3^o	18%	7.6%	5%	5%	5%	5%	10%
1	Slab-only	20	1.5	50	610	11.9	4.02	0.43	0.0581	0.0487	1.452e-4	0	∞
2	Slab-only	20	1.5	50	566	19.1	3.53	0.41	0.0718	0.0613	2.153e-4	0	∞
3	Slab-only	20	1.5	60	836	14.5	–	0.59	0.0910	0.0764	2.731e-4	0	∞
4	Front-plume (B)	20	1.5	50	610	20.9	3.99	0.45	0.0579	0.0474	1.736e-4	1.739e-6	99.89
5	Front-plume (B)	20	1.5	50	640	14.6	4.64	0.46	0.0569	0.0462	1.706e-4	4.322e-6	39.48
6	Front-plume (B)	20	1.5	50	593	16.3	4.19	0.42	0.0625	0.0520	1.875e-4	7.164e-6	26.18
7	Front-plume (B)	20	1.5	50	566	24.8	3.38	0.43	0.0739	0.0606	2.217e-4	1.405e-5	15.78
8	Front-plume (A)	20	1.5	60	566	24.0	3.45	0.43	0.0708	0.0601	2.123e-4	1.422e-5	14.93
9	Front-plume (B)	20	1.5	60	627	20.5	4.06	0.46	0.0589	0.0495	1.766e-4	1.413e-5	12.50
10	Rear-plume (C)	20	1.5	60	593	16.8	4.15	0.43	0.0634	0.0555	1.901e-4	7.569e-6	25.12
11	Rear-plume (C)	20	1.5	60	538	36.7	3.76	0.49	0.0725	0.0608	2.175e-4	1.755e-5	12.39
12	Rear-plume (C)	20	1.5	60	538	36.7	3.77	0.47	0.0720	0.0607	2.159e-4	3.264e-5	6.61
13	Rear-plume (C)	20	1.5	60	842	19.8	–	0.61	0.1018	0.0876	3.054 e-4	7.424e-5	4.11
14	Rear-plume (C)	20	1.5	60	810	16.8	–	0.58	0.0921	0.0797	2.764e-4	7.633e-5	3.62
15	Rear-plume (C)	20	1.5	60	842	17.2	–	0.61	0.0910	0.0743	2.726e-4	7.854e-5	3.47
16	Rear-plume (C)	20	1.5	60	865	20.7	–	0.64	0.0923	0.0735	2.769e-4	8.035e-5	3.44
17	Rear-plume (C)	20	1.5	60	780	22.6	–	0.58	0.0891	0.0783	2.674e-4	9.109e-5	2.93
18	Rear-plume (C)	20	1.5	60	847	11.6	–	0.60	0.0972	0.0837	2.864e-4	1.264e-4	2.26
19	Side-plume (E)	20	1.5	60	593	18.8	4.02	0.43	0.0611	0.0529	1.845e-4	7.086e-6	26.05
20	Side-plume (D)	20	1.5	60	566	26.8	3.22	0.44	0.0771	0.0647	2.312e-4	1.22e-5	19.07
21	Side-plume (E)	20	1.5	60	538	20.3	3.41	0.39	0.0704	0.0581	2.111e-4	1.297e-5	16.27

Table 1: Model dimensions (see also Appendix S1).

3. Results

We present experiments that include different initial positions of the plume relative to the slab and different buoyancy flux ratios B_s/B_p. We catalogued the relative plume positions into three classes: the front, rear and side plume positions, respectively (see Table 1 and Figure 1). The plume was initiated at a time $t_p^i = 20$ s after subduction of the plate had been initiated, except for experiments 13, 15, 16 and 18, for which the plume was started at t_p^i =610, 330, 700, and 250 s, respectively, after subduction initiation.

In all experiments, slabs first steepened with time (up to $\sim$ 90 degrees for the bottom half of the slab, and then steadily sunk and retreated while attaining a dip angle of $\sim$ 50 degrees (e.g. Figs. 2-4). Slabs were also seen to curl along their lateral edges in response to the drag of the surrounding mantle, producing a top-view curvature that is concave towards the mantle wedge. Finally, as the slab tip approached the bottom of the tank, slab rollback and slab sinking decelerated. This subduction process induces a flow in the mantle that can be decomposed into slab-induced toroidal and slab-induced poloidal components (see Strak and Schellart (2014) for stereoscopic Particle Image Velocimetry of slab-induced 3-D mantle flow). These two components vary in space and time as the slab lengthens. In particular, the slab-induced flow is characterized by the two poloidal circulations in the mantle wedge and sub-slab domain, and the two toroidal cells around the lateral slab edges (see Figure 1). In our experiments, the extent of the slab-induced poloidal and toroidal circulation at the surface were estimated as a function of slab length using the neutrally buoyant tracers that had been seeded at the surface (Appendix S2.1).

3.1. Generic Front, Rear and Side plume experiments 6, 10 & 19

We qualitatively detail here experiments 6, 10 & 19, which model three plume positions, front, rear and side, relative to the plate for a similar buoyancy flux ratio $B_s/B_p = 25.78 \pm 0.58$.

3.1.1. Front plume experiment 6

The plume was initiated at the apex of the slab tip. It took about 200 s for the plume head to grow and lift up from the bottom. The plume then rose vertically for about 250 s until it started to be deflected away from the slab due to the slab-induced poloidal circulation in the wedge. This deflection continued until the plume head reached the height of the slab tip at a time of 670 s (Figure 2a, 2b & 2c). At this stage, the plume head was still fairly axisymmetric; the plume and slab tip were 9 cm apart. Beyond this time, the plume head and upper part of the conduit began to be increasingly advected towards the slab and trench by the poloidal circulation, and the plume head became elongated in the direction perpendicular to the trench (Figure 2d, 2e & 2f). During this late stage, the plume deformation also resulted from the mantle return flow due to the slab's rollback motion dominated by the toroidal component. In particular, it resulted in the plume head being pinched at its end. A movie named Movie-Front-Plume showing the dynamics of the interaction over time is provided in the Appendix.

3.1.2. Rear plume experiment 10

The plume was initiated underneath the slab 17.5 cm away from its tip. The plume rose vertically for 640 s. The influence of the slab started when the slab tip and the plume head reached the same vertical position. Due to

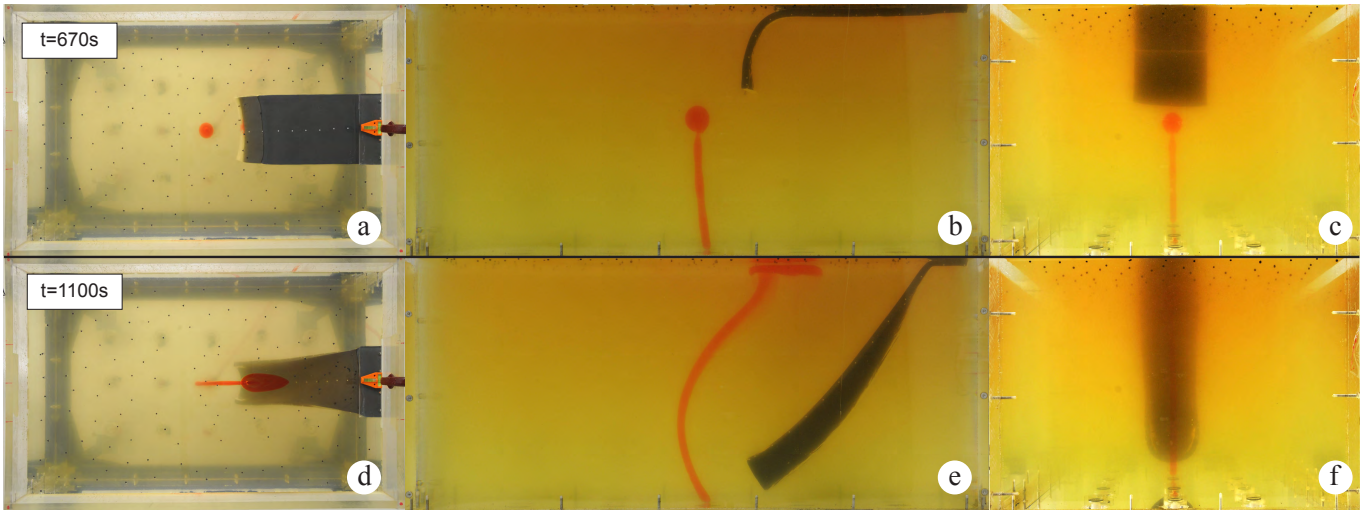

Figure 2: Two stages of the front-plume experiment 6 showing the slab/plume interaction at t=670 s (top frames a, b and c) and 1100 s (bottom frames d, e and f). The three top and bottom frames represent the top, along (side) and across (front) slab views from left to right, respectively.

the slab-induced poloidal circulation,the plume head then began to develop an asymmetry pulling down its left side, and the conduit got slightly bent as shown in the Figure 3b. Thereafter, the plume got further swept away by the slab during its rollback motion. Significant flattening of the plume in the direction perpendicular to the slab plane (and elongation parallel to the trench), including its head and its conduit, occurred during this phase due to slab-induced toroidal flow, as is shown in Figure 3f. Ultimately, the whole plume underplated the slab (this can be seen in the movie provided in the Appendix named Movie-Rear-Plume).

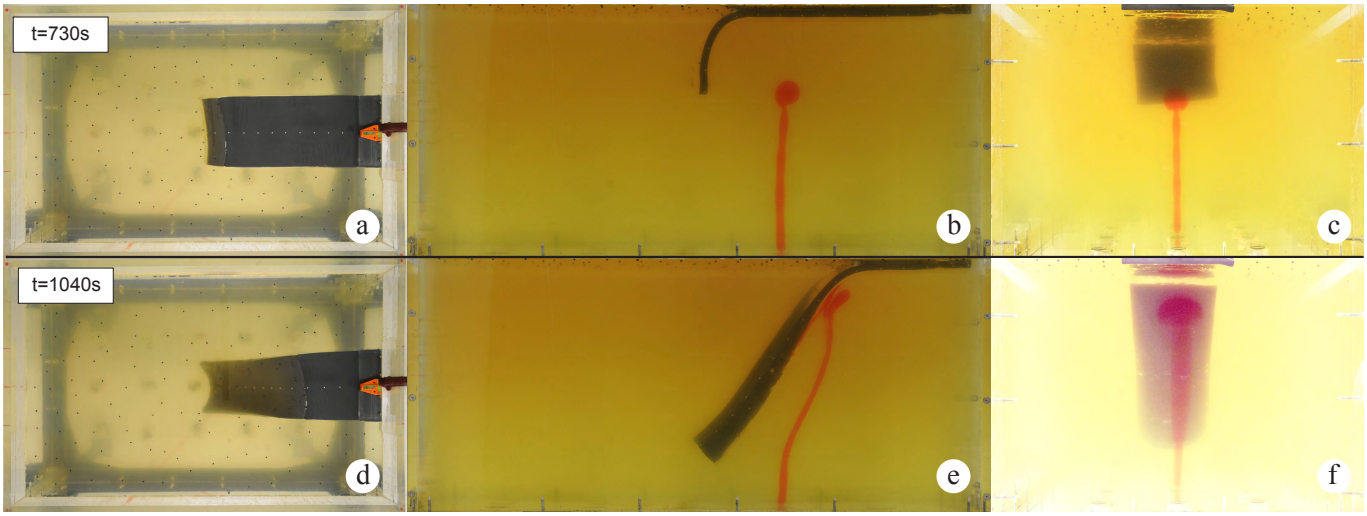

Figure 3: Two stages of Rear-plume experiment 10 showing the slab/plume interaction at t=730 s (top frames a, b and c) and 1040 s (bottom frames d, e and f). The three top and bottom frames represent the top, along (side) and across (rear) slab views from left to right, respectively. We note that the color scheme in frame f was modified to enhance the plume visibility.

3.1.3. Side plume experiment 19

In experiment 19, the plume was initiated 17.5 cm at the rear of the initial slab tip, and on the side of the slab 16 cm away from its centreline. For 630 s, the plume rose while very slightly tilting by 1.1 degree towards the slab as shown in Figure 4a, 4b & 4c. The plume head became very slightly asymmetric. At this stage, the slab tip and the plume head had not yet reached the same vertical position. As the trench arrived in the vertical plane of the plume, the latter started a clockwise rotation under the influence of the slab-induced toroidal flow, before being further dragged towards the trench by the slab-induced poloidal flow in the mantle wedge, as shown in Figure 4d, 4e & 4f. This process occurred in about 460 s, scaling to 3 Myr.

A movie named Movie-Side-Plume is included in the Appendix.

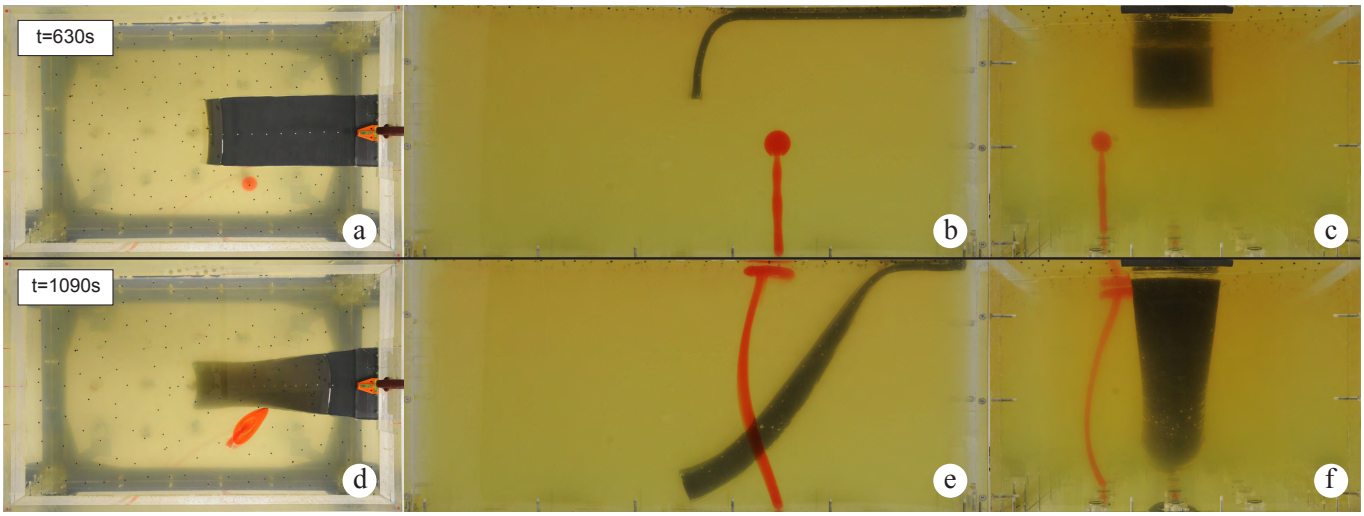

Figure 4: Two stages of the Side-plume experiment 19 showing the slab/plume interaction at t=630 s (top frames a, b and c) and 1090 s (bottom frames d, e and f). The three top and bottom frames represent the top, along (side) and across (rear) slab views from left to right, respectively.

3.2. Slab sinking rates

As the plate is not motor-driven but left to sink on its own, the slab sinking rate is not *a priori* known and requires an *a posteriori* analysis. We used the side-view photos to analyze the tip position with time. An initial transient phase that will be further discussed in section 3.3.1 is seen across all experiments. This phase, whose sinking regime is in a stiffness dominated regime (see Appendix S2.2), slightly varies between experiments due to unavoidable slight differences in the tip initiation. However, beyond this phase all experiments exhibit a steady linear sinking rate of the tip U, until the tip approaches the bottom of the tank. The slab steady sinking rate

was determined by linear fits on the slab tip positions as a function of time in the interval between the initial transient, typically after 500 s, and before the slab deceleration as it approached the bottom. As the plate was subjected to some transverse deformation during its sinking, we measured the sinking speed of the slab's at its centre U and at its lateral edge U_{edge}. The middle of the slab systematically sunk faster than its sides with U being larger than U_{edge} by 10% to 19% (Table 1). These results are consistent with those of Li and Ribe (2012) whose difference in sinking speeds was up to 20%.

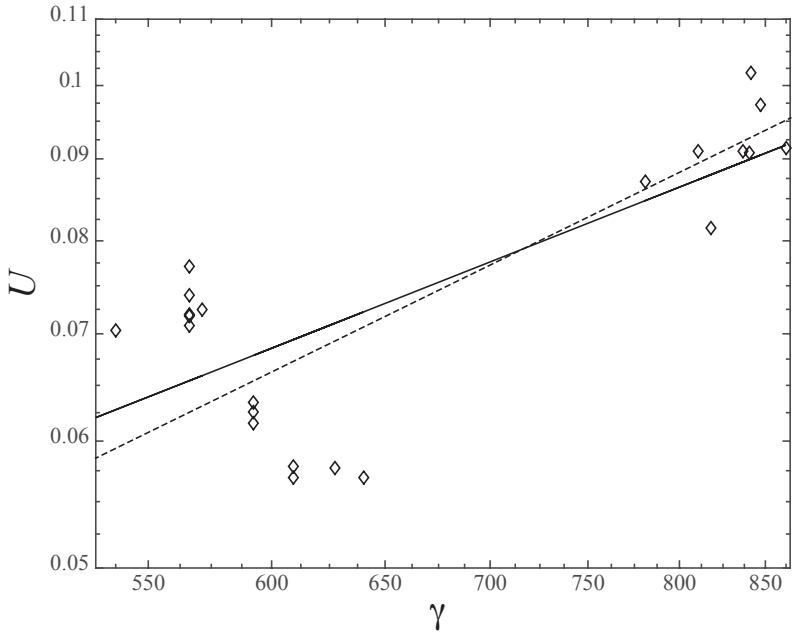

Figure 5: The slab tip sinking rates. Log-log plot of sinking speeds U as a function of $\gamma = \mu_s/\mu_a$. The straight black line is the fit obtained for all experiments by linear regression, whose slope is 0.80 and root mean squared error is 0.13. The dashed black line is the fit obtained for experiment 3, 6, 10 & 13-19 by linear regression, whose slope is 0.99 and root mean squared error is 0.05.

Figure 5 shows the steady sinking rates U as a function of γ on a log-log scale for all experiments. We find that there is a general trend for a decrease of the velocity as γ increases. The slope of the fit obtained by linear regression is not strictly 1, as expected in the Stokes regime, but 0.8 with a root mean squared error of 13.5%. However, if we consider experiments 3, 6,10 & 13-19 only, the sinking velocity U appears to vary more convincingly as μ_a^{-1}, equivalently γ, as the fit obtained by linear regression has a slope of 0.99 with a root mean squared error of 0.05. We note that a similar fit by linear regression for the experiments 1-2, 4-5, 7-9, 11-12 & 20-21 does not give a slope of 1 but -2. In part, this can be attributed to the errors made in measuring the viscosity of order 5%, but this is not sufficient to explain some apparent errors of the viscosity of 12-24% for experiments 1-2, 4-5, 7-9, 11-12 & 20-21. So it seems that, for the latter experiments, the sinking rate variations would not be explained by the viscosity variations alone. Some influence of the initial conditions cannot be excluded. Based on dimensional analysis, Li and Ribe (2012) for example predicted that U would be a function of θ_0, even though such a dependency is not perceived through our values of U and θ_0.

3.3. Impact of buoyancy flux ratio and plume positioning

3.3.1. Plume influence on slab subduction

The previous sinking rate analyses were performed regardless of the buoyancy flux ratio B_s/B_p. In other words, the changes in sinking rates were not attributed to plume buoyancy but rather to viscosity and, to a lesser degree, initial conditions variations. For instance, the sinking rates of the slab in the front, rear and side plume experiments 6, 10 & 19 and slab-only experiment

1, which had a similar initial plate stiffness $S_0 = 4.06 \pm 0.13$ (Appendix S2.2, equation 2), and a similar buoyancy ratio $B_s/B_p = 25.78 \pm 0.58$, when in the presence of a plume, differed by only 4% although the initial transients occurred over varying time intervals from 610 s to 760 s (i.e. a time difference $\delta t_i = 150$ s), times at which the slab had typically reached 12 cm (600 km) (Figure 6a). Similarly, experiments 2, 7, 8, 11 & 21 of buoyancy flux ratio $B_s/B_p = 14.84 \pm 1.72$ and $S_0 = 3.51 \pm 0.15$, and whose transients time varying from 490 to 640 s had a similar $\delta t_i = 150$ s and similar slab lengths of $\approx$ 12 cm, had sinking rates that differed by no more than 2% (Appendix Figure S2.2). At those buoyancy flux ratios, there was thus no plume influence on the slab to be found.

By contrast, at lower buoyancy ratios $B_s/B_p \sim 3$ (experiments 13-16 & 18), although the sinking rates were all consistent, the initial transient phase showed a lot more variability as shown in Figure 6b. The extent of such variability cannot be explained by differences in the initiation alone. In particular, experiment 14 did not start to sink at a steady rate before 830 s, a transient time 1.4 times longer than the transient time of experiments 3, 13, & 16, spanning a time interval of $520 - 670$ s, at which slabs were all ≈ 12 cm long. In fact, over much of its transient, the plate was subjected to the force of a strong plume that started to spread axisymmetrically underneath the plate while the slab was only 4 cm long. The plume thus postponed the subduction process for at least 150 s ($\sim$ 1.3 Ma). In experiment 18, the strong plume did postpone subduction for only ≈ 50 s because it afterwards started to underlie the slab, as the latter was already 8 cm long, hence close to the 12 cm threshold for steady sinking. The transient phase of experiment

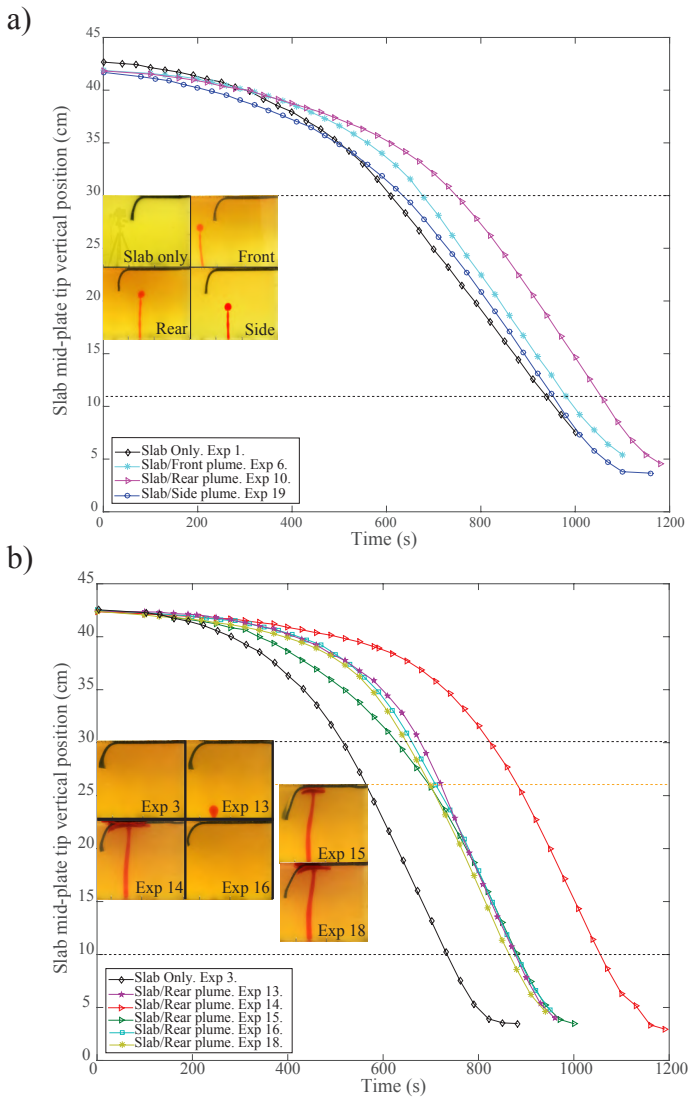

Figure 6: Slab tip vertical positions as a function of time. a) Slab only experiment 1 and, slab and Front, Rear and Side plume experiments 6, 10 & 19, respectively. b) Slab only experiment 3 and, slab and Rear plume experiments 13-16 & 18, respectively. The two black dashed lines indicate the two vertical positions between which linear regressions on the slab tip positions were made to determine the slab steady sinking rates U given in Table 1. For experiments 15 and 18, the linear regression started at a greater depth (at the level of the orange dashed line). The ten inserts show the slab and plume positions from where the linear regressions start.

15 was also peculiar. It lasted 700 s while a strong plume underlay the plate from a time of 610 s, where the slab was 12 cm long ready to begin its steady sinking phase. The plume halted it for 90 s ($\sim$ 0.8 Ma). Interestingly, the plume initial impact in experiment 15 was closer to the plate bend at 12 cm compared to 20 cm away in experiments 14 and 18. Plumes in experiments 14, 15 & 18 thus interfere with the plate bending as they represent a sufficient net vertical shear force

$$F_p = \Delta\rho_p (Q/A_p)^2, \tag{4}$$

where A_p is the area of the plume underneath the plate, opposing the vertical traction due to the plate negative buoyancy,

$$F_b = \Delta\rho_s g d l W. \tag{5}$$

Estimates of F_p and F_b at the time of plume spreading initiation underneath the plate show that F_p/F_b ratios were 29%, 22% and 21% for experiments 14, 15 & 18 respectively (see Appendix Table S2.2). Note that F_p/F_b ratios are consistent with experiment 14 having the most plume influence on bending. Although involving strong plumes, experiments 13 & 16 did not show a modified subduction because plumes interacted with slabs of increasing lengths, and hence of greater F_b. In particular, these strong plumes did not modify the slab's dip angle. This work modelling subduction in a whole mantle contrasts with that of recent upper-mantle models (Mériaux et al, 2015b) for which F_b was limited by the model depth. Nevertheless subduction can be slowed down in both cases, during the bending phase in the first case, and during the steady retreat in the second case. Furthermore, in these experiments, strong plumes could spread axisymmetrically underneath the plate as

the slab was initiated, but then preferentially spread towards the trench as the slab-induced poloidal flow established itself (see also the supplementary information, Mériaux et al, 2015b).

3.3.2. Plume head asymmetry & flattening

In all experiments, plume head asymmetry develops. Front plumes were elongated in the trench-normal direction by the slab-induced poloidal flow component in the mantle wedge, side plumes were elongated in a direction oblique to the trench axis by the slab-induced mixed poloidal and toroidal flow components in the sub-slab/mantle wedge transition region (see Figures 2 & 4). Rear plumes were elongated in the trench-parallel direction due to flattening in the trench-normal direction by the slab-induced toroidal flow component (see Figure 3), unless they had reached the surface before the slab had lengthened enough to generate efficient toroidal flow. This happened in experiments 14, 15, 17 & 18, which had a high buoyancy plume relative to the slab, but not experiments 13 and 16 because of the delay in plume initiation. Figure 7 shows that trench-normal flattening started as the slab-induced toroidal flow component could influence the plume, which occurs when the plume and the slab reach the same height, highlighted by arrows in Figure 7. The amount of flattening linearly increased with the retreat rate, and hence the magnitude of the slab-induced toroidal flow component.

Once underneath the slab, on-going flattening of rear plumes actually led to increased plume volume as the plume buoyancy increased. In experiments 10, 11, 12 and 18, sorted by increase buoyancy, the surface area of plume fluid underneath the slab was 39%, 56%, 79% and 87% that of the slab, respectively, at the end of each experiment. So the slab is eventually

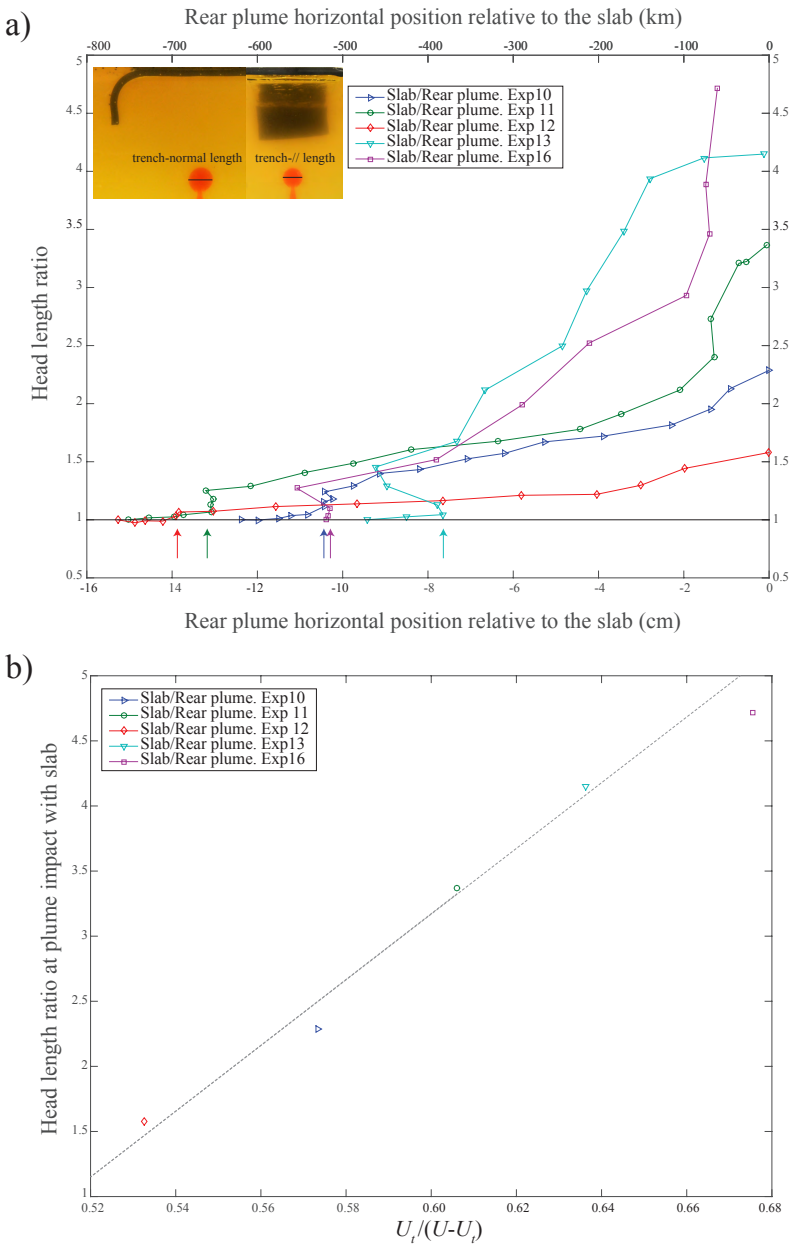

Figure 7: a) Ratio of the trench-parallel (from rear view) by the trench normal (from along view) lengths of the plume head as a function of distance between the slab and the plume measured at plume head mid-height for rear plume experiments 10-13 & 16. Each arrow indicates the distance at which the plume reached the slab depth. b) Ratio of the trench-parallel (from rear view) by the trench-normal lengths of the plume head when the slab reaches the plume as a function of dimensionless retreat rate $U_t/(U-U_t)$ with $U_t < 0$. The black dashed line shows the linear fit.

almost underlain by a fluid of lesser density and viscosity. Interestingly, the slab sinking rate is not seen to be sensitive to such a lesser viscous layer or "ambient" as the sinking rate is not seen to increase.

3.3.3. Tilt initiation & Maximum tilt

The slab/plume interaction can take place even when slab and plume are far apart. This is especially true for front plumes which are sensitive to the slab-induced downwelling associated with the poloidal circulation in the mantle wedge. In experiments 4, 5, 6 & 7, due to such downwelling, plumes started tiltingtowards the mantle wedge at increasing depths as the slab/plume buoyancy ratio was increased. Plumes thus reached a tilt of three degrees (equivalent to a horizontal displacement of 2.36 cm or 118 km over a depth of 45 cm or 2250 km, respectively) at a distance from the slab tip of 5 cm (250 km), 11 cm (550 km), 18 cm (900 km), and 27 cm (1350 km) as the slab/plume buoyancy flux ratios of experiments 4, 5, 6 & 7 increased from 16 to 26, 39 & 100, respectively (see Appendix S2.5).

In contrast, for the side and rear plume positions, tilting of the plume began when plume and slab were at about similar depths regardless of B_s/B_p. During the experiments, the plume tilt varied in time and space, and could be substantial as for experiment 8, which exhibited a plume conduit tilted by as much as 66^o (Appendix Figure S2.4).

3.3.4. Plume material capture in the mantle wedge

In a retreating subduction mode, regardless of the initial plume position, the slab-induced toroidal flow is very efficient at capturing plume material in the mantle wedge as shown in Figure 8. In experiments 8, 9, 18 & 21,

plume material even started to be subducted towards the end of slab retreat. In experiment 18 (Figure 8), the slab at the end of the experiment was also wrapped at depths by plume material, down to about 28 cm (1400 km). Front plumes that are of lesser buoyancy and under a greater influence of the combined slab-induced poloidal and toroidal flow due to their proximity to the slab during their ascent (e.g., in experiment 8, at its arrival at the surface, the plume is $\sim$ 9 cm (450 km) apart from the trench) can be entirely dragged towards the trench along a line (Figure 8, top left frame). By contrast, plumes of higher buoyancy and further away from the trench (e.g. in experiment 9, at its arrival at the surface, $\sim$ 16 cm (800 km) separates the plume and the trench) can keep memory of the purely axisymmetric spreading in the limit of no-ambient shear or infinitely buoyant plumes (Figure 8, top right frame).

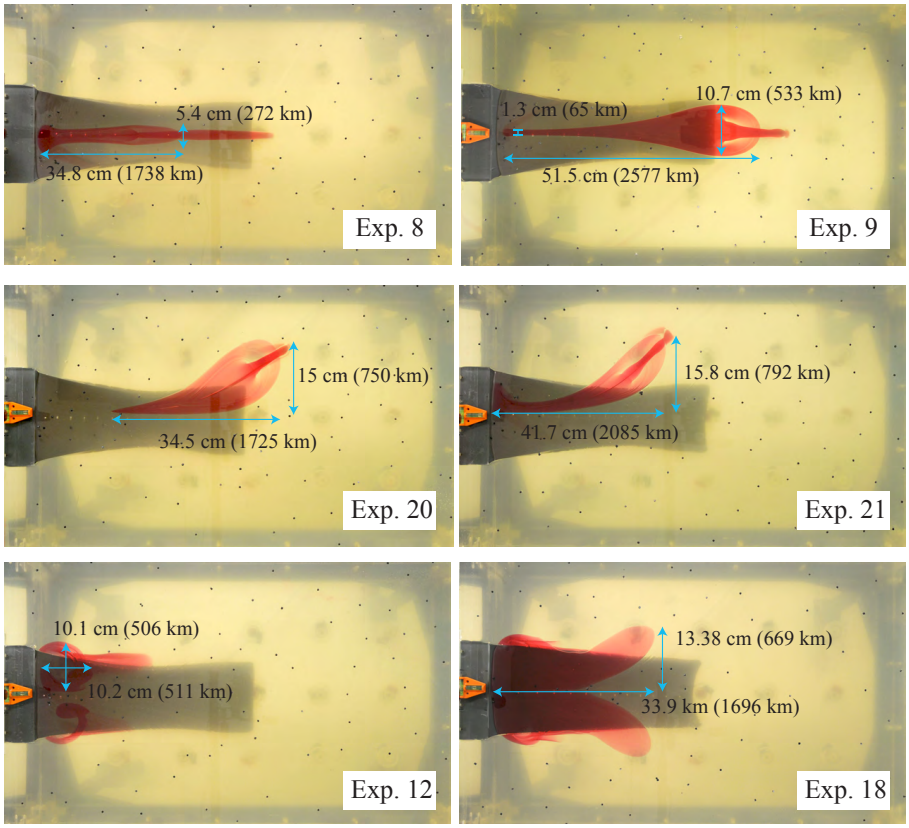

Figure 8: Plume material distribution after interaction with a retreating slab. Top frames are front plume experiments 8 & 9, from left to right, respectively. Middle frames are side plume experiments 20 & 21, from left to right, respectively. Bottom frames are rear plume experiments 12 & 18, from left to right, respectively. The blue arrows indicate the horizontal extent of plume material at the surface. The plume lateral spreading at the surface is influenced by both the slab-induced poloidal and toroidal flow components. This shows that the spatial distribution of mixed plume-arc-related magmatism could actually be extremely variable, and depending on the plume position relative to the slab, could be found from along a line to within a pear shape region or torus in the mantle wedge.

3.3.5. Sensitivity of slab/plume relative position

Varying the proximity between plume and slab within the same region can have its importance. This is best shown by experiments 7 & 8. These two front plume experiments differed by only 5% in B_s/B_p but differed by their plate lengths of 50 and 60 cm, respectively. The subsequent slightly different initial position of the plume relative to the slab (Appendix Figure S2.5) later resulted in a closer proximity of the plume and the slab. In addition, compared to experiment 7, the plume in experiment 8 rose at a slower rate as shown in Figure S2.5 due to a much greater influence of the slab-induced downwelling associated with the poloidal circulation in the mantle wedge.

4. Discussion

4.1. Application to nature

The range of plausible slab/plume buoyancy flux ratios B_s/B_p in nature today is 0.2–710 (see Appendix Table S3.1). Apart from its lowest and highest bounds, our experiments are within a range of 2-100, which overlaps the range in nature. The dynamics of subduction systems on Earth is commonly classified into three modes that differentiate by their absolute motion of the trench: a retreating mode, an advancing mode, and a quasi-stationary mode (Schellart et al., 2008). In effect, these three modes differ in their partitioning of the poloidal and toroidal flows. Plume deflection being a response to the poloidal and toroidal flows will thus differ across the different subduction modes. However, the retreating mode is the most frequent mode (Schellart et al., 2008). Long-term trench advance and slab roll-forward appear nonexistent on Earth as slab roll-over geometries do not exist on Earth (Ribe,

2010). In our experiments, we model a retreating mode that generates significant toroidal mantle flow providing a mechanism for mantle plume material to be dragged towards the mantle wedge. By contrast, a quasi-stationary subduction mode will be dominated by the poloidal circulation that keeps the plume material in its original domain due to the absence of mass flux between the sub-slab and wedge regions (Figure 2; Kincaid and Griffiths, 2003). Our experiments also model a deep mantle, so the poloidal circulation is important. *Sensu stricto*, our experiments thus apply to slabs that would pass through the 670 km discontinuity. Systems with shallow slabs would retain a similar dynamics as that of whole mantle systems but with enhanced toroidal flows due to the viscosity interface (Royden and Husson, 2006).

4.2. Modern plumes in the vicinity of subduction zones

As of today, there are a number of plumes among the catalogues of Sleep (1990), Montelli et al. (2006), Courtillot et al. (2003) in proximity of a subduction zone. If such proximity is a necessary condition for interaction, it is certainly not sufficient. Each potential system thus needs to be discussed on a case-by-case basis. Some systems have already been shown to bring together all the conditions for interaction. These are Cascadia/Yellowstone over the last 30 Myr (Kincaid et al., 2013), Tonga/Samoa (Druken et al., 2014), Gibraltar/Canary (Mériaux et al., 2015a), and Manila/Hainan (Mériaux et al., 2015b), and we refer to these publications for a detailed discussion of these systems. We describe below the case of four Pacific hotspots in the vicinity of a subduction zone (Figure 9).

In the Northeastern Pacific, the Bowie hotspot is part of the 900 km-

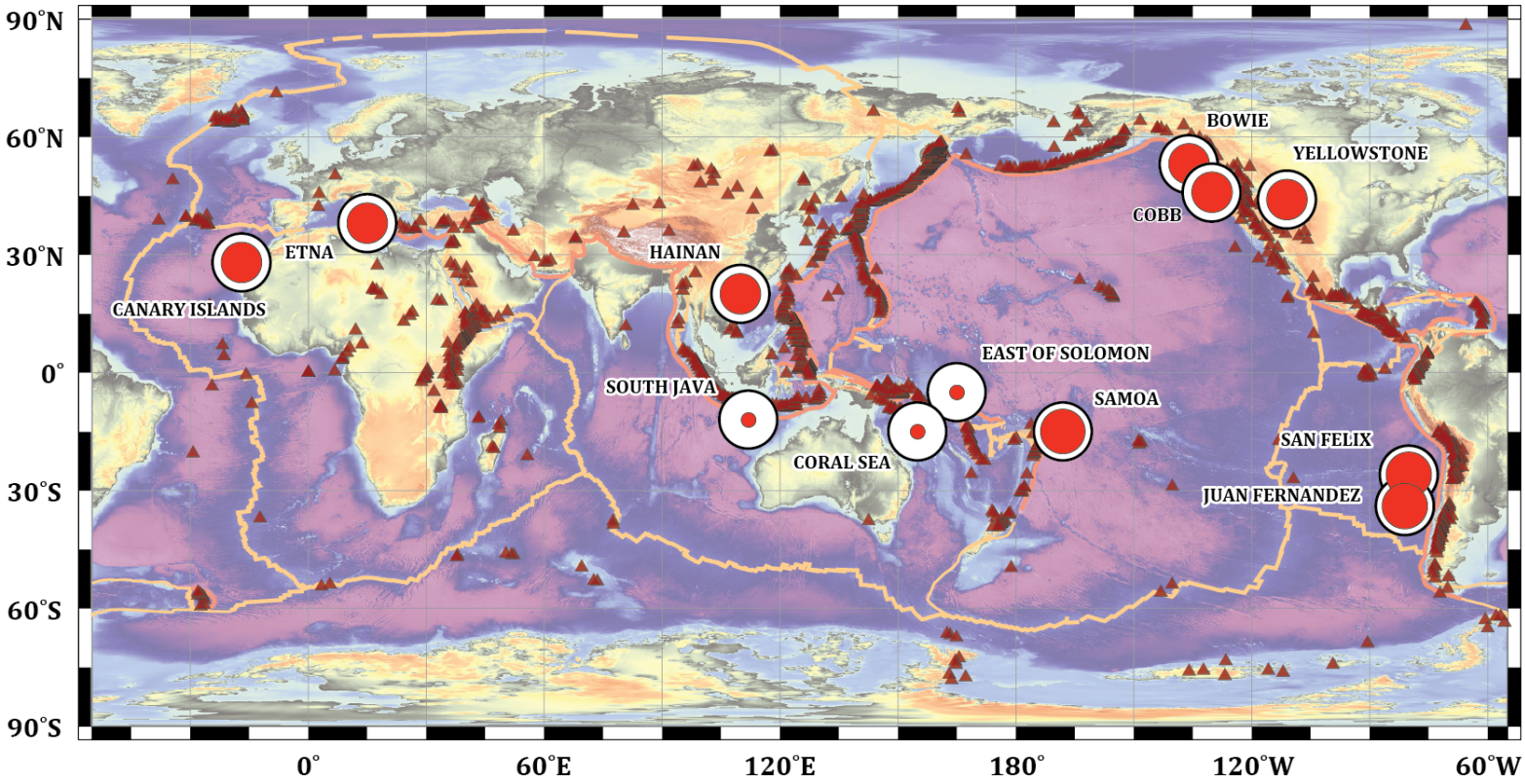

Figure 9: Selected modern plumes close to a subduction zone, either recently studied or discussed in this paper. Mantle plumes that do not reach the surface (white circles) are distinguished from those seen at the surface (red circles).

long Kodiak-Bowie seamount chain. The ages of the seamounts are typically younger at Bowie ($\geq$0.7 Ma) than at Kodiak (up to 24 Ma) and essentially reflect movement of the Pacific plate over the Bowie hotspot (Chaytor et al., 2007). Parallel to this chain, the Cobb seamount chain extends from the current location of the Cobb hotspot on the Juan de Fuca ridge to the 26 Ma Marchand Seamout, just oceanward of the Aleutian trench (Chaytor et al., 2007). Both chains could well be older than $\sim$ 20 Ma as seamounts at the termination of those tracks may have disappeared with the subduction of the Pacific plate beneath Alaska over the last 60 Ma (Von Huene et al., 2012; Heuret and Lallemand, 2005). Today Bowie is about 160 km west of the Queen Charlotte transform Fault, a fault activated 30 Ma ago, and 320 km northeast of the northern termination of the Cascadia subduction zone, from where the Juan de Fuca rigde sinks under the North American plate (see Appendix Figure S3.1). The Cascadia subduction where the Juan de Fuca plate, a remnant of the Farallon plate, is shoved underneath the North American plate is today characterized by a southwestward trench retreat of about 2.2-3.1 cm/yr for a convergence rate of the slab of about 4.4 cm/yr (Schellart et al., 2011). In effect, Bowie could be considered in a side/rear position relative to the retreating Cascadia trench (equivalent, in the laboratory, to a position 6 cm from the plate edge and 2.7 cm at the rear of the trench parallel direction and a buoyancy flux ratio of about $\sim$5, see Appendix Table S3.2). Yet, despite such proximity and buoyancy flux ratio, a present-day interaction is unlikely because Bowie and the Cascadia subduction are disconnected by an active mid-oceanic ridge, the Juan de Fuca Ridge, whose spreading is occurring at a half-rate of about 2.9 cm/yr (5.8

cm/yr total), in the direction parallel to the WNW-ESE fracture zones (e.g. Atwater, 1970). Today the Bowie plume material is thus more likely to be either entirely deflected away from the ridge by the Pacific plate flow or divide itself into one part migrating toward the ridge and the other part being deflected away from the ridge (Kincaid et al., 1995). Similarly, despite of its close position ($\sim$ 330 km) at the rear of the Juan de Fuca retreating slab and buoyancy flux ratio of $\sim$10 (Appendix Figure S3.1 and Table S3.2), the Cobb hotspot has been under mid-oceanic ridges over the last 45 Ma, which excludes the possibility of slab/plume interaction during this period (see the movie PlateKinematic-HS-since60Ma.m4v provided in the Appendix).

In the Southeastern Pacific, the San Felix and Juan Fernández hotspots, $\sim$ 930 km apart, are located 820 and 835 km, respectively, west of or at the rear of the shallow South-American subduction zone (Figure 9 and Appendix Figure S3.2). Compared to Bowie and Cobb hotspots characterized by a buoyancy flux of 600 kg/s and 300 kg/s, respectively, San Felix and Juan Fernández are stronger hotspots with buoyancy fluxes estimated at 1600-2300 kg/s, and 1600-1700 kg/s, by Sleep (1990) and Davies (1988), respectively. These plumes could be considered at the rear of a continuous 6000 km-wide Nazca plate subducting at a rate of $\sim$ 7 cm/yr beneath the South America plate with a retreat rate representing $\sim$10 to 25% of the subduction velocity (Schellart et al., 2011), and a shallow depth of the slab (between 140 and 600 km). In this way, the Nazca/San Felix and Nazca/Juan Fernández systems would be characterized by a similar buoyancy flux ratio B_s/B_p of $\sim$ 17 (Appendix Table S3.2), suggesting a slab dominated interaction.

With very limited mass flux between the sub-slab and wedge regions

following the quasi-stationarity of the trench, this subduction is to favour the poloidal flow in the sub-slab region, and consequently the tilting the plume towards the trench in the upper mantle some distance away from the trench, Additionally, regardless of retreat rates, the slab is in places very shallow, which does not promote slab-induced toroidal flow. In our experiments, short slabs do not generate toroidal flow that can be detected either from plume deflection or from the buoyant tracers displacement (Appendix S2.1). The limited slab-induced toroidal flow in the upper mantle actually appears consistent with the global tomography models showing a deflection of both plumes towards the east in the upper mantle rather than the west (Zhao, 2007; Pesicek et al., 2012).

Now, whether the Andean slab is assumed continuous for $\sim$ 6000 km or segmented by slab windows and tears (Russo and Silver, 1994; Thorkelson et al., 2011), as currently debated, could lead to a different interaction with the San Felix and Juan Fernández plumes. Today, the Juan Fernández hotspot is aligned with the Juan Fernández ridge that is subducting obliquely under South America and likely causes the flattening of the slab as observed for the Nazca ridge further north. As to the young $\sim$ 3 Ma San Felix hotspot (Clouard and Bonneville, 2005), it is located between the Nazca and Iquique south migrating fossil ridges (Figure S2). In addition, while San Felix faces the well-developed 910-km wide slab of the hinge of the Andean Orocline, imaged by earthquakes to great depths (up to $\sim$ 600 km, Figure S2), Juan Fernández is at the rear edge of a much shallower ($\sim$ 140 km deep) and wider (2940 km) slab segment adjacent to a flat slab segment to the north. Integrating such segmentation would change the buoyancy flux ratios of the San

Felix/Nazca and Juan Fernandez/Nazca to $B_s/B_p \sim 3$ and 10, respectively (Appendix Table S3.2), and increase the roles of these plumes. In such a geodynamic context, breaches of the Nazca slab in the region might develop offering a direct path for the transfer of plume material to the mantle wedge, similarly to the ridge-plume-slab scenario modelled by Betts et al. (2015) but with a more complex slab geometry. Furthermore, even if, in the first instance, the slab would keep its integrity and accommodate the deformation by flexure alone, sub-slab grooves would develop and host plume channel flows that would promote mechanical erosion, and possibly, the segmentation of the South American slab. In other words, the oblique convergence of fossil ridges together with the Pacific plumes of San Felix and Juan Fernández could lead to the tearing of the Nazca slab and hence a significant mantle flow reorganization in the southern Pacific.

4.3. Some implications

4.3.1. Long-range interaction

Our retreating slab mode experiments demonstrate that the slab/plume interaction operates at long-range. Thanks to the poloidal circulation, plume material can be captured at a distance of 885 km from the trench (Front plume Exp. 9) and then dragged in the mantle wedge over 2700 km towards the trench (Front plume Exp 9; Figure 8). Also, as discussed in section 3.3.3, whereas side and rear plumes would start being deflected when plume and slab are at about similar depths regardless of buoyancy flux ratio, front plumes could be tilted at great depths by slab-induced downwellings, the depth of influence increasing with the plume "weakness". This behaviour is especially expected for the starting plume that is only visible in the lowermost

mantle up to 1900 km depth beneath the region East of Solomon (Montelli et al., 2006). Although the plume buoyancy is unknown, and the central San Cristobal segment is nearly stationary, a northeast tilt could be expected in the lower mantle due to slab downwelling. In contrast, the starting plume South of Java (seen up to 1450 km depth) (Montelli et al., 2006) being at the rear of the retreating Java subduction segment at $\sim$ 2 cm/yr southward should be less influenced at depths by the slab downwelling given the shallow slab depth. Provided that this subduction zone is stable, the interaction with this plume will start when the slab and plume reach similar depths. The starting plume in the Coral sea (seen up to 550 km depth) (Montelli et al., 2006), being at the rear of both retreating New Hebrides (slab depth $\sim$ 400 km) and New Britain (slab depth $\sim$ 600 km) subductions, at rates of $\sim$ 4-5 cm/yr westward and southeastward, respectively (Schellart et al., 2011), would reflect such an interaction initiation. The long-range character of slab/plume interaction, both at depth, and at the surface, also implies that coeval plume and arc magmatism could be linked while being spatially separated, as shown by Heron et al. (2015) linking the large igneous province positions with paleosubductions over the last 300 Ma.

4.3.2. Plume-arc magmatic regions

A variety of slab/plume interactions have been inferred from the presence of simultaneously arc-related and plume-related magmatism and contrasting geochemical signatures (see Appendix Table S3.3). While modern examples can benefit from the insights of tomography, past examples have been relying on additional plate reconstructions only. Our experiments suggest that the spatial distribution of mixed plume-arc-related magmatism could actually be

extremely variable in the event of an interaction (see Figure 8 in a rollback subduction mode). Still our study provides for retreating slabs three clues to corroborate slab/plume interaction. First, a plume at a rear of a subduction zone or close to the lateral edge of a retreating slab can emerge in the mantle wedge, and thus imprint the magmatic arc. Second, plumes at the front of the subduction zone can be captured by the efficient poloidal flow at long range distances (up to 2500 km), and similarly mix with the arc volcanism. The third clue is the lateral plume spreading in the mantle wedge: The larger the plume buoyancy flux, the more trench-parallel plume spreading, whereas the closer the plume to the trench, the less trench-parallel plume spreading.

5. Conclusion

In this study, we have shown that slab/plume interaction is far from being trivial but can develop into many scenarios. First, buoyant plume material can underlie a slab over much of its area after slab/rear plume impact following flattening of the plume in the trench-parallel direction during slab retreat. Second, weak plumes can potentially be tilted at great depths when under the influence of a slab downwelling in the mantle wedge. Third, plume material can be captured at long-range distances, which can lead to a diversity of potential plume source material distributions in the mantle wedge that will ultimately be superimposed with arc magmatism. Last but not least, rear plumes of sufficient buoyancy flux can halt subduction in the upper mantle. Today there is no record of such event, but in the Archean period, during which mantle plumes are thought to have been very strong, such a scenario cannot not be ruled out, and it remains to be seen what the additional upper

mantle stratification would do in such a case. We hope that our study will prompt more systematic investigations of the interaction.

6. Acknowledgment

The present work was supported by the Fundação para a Ciência e a Tecnologia under the Project iPLUS-PTDC/CTE-GIX/122232/2010. CM acknowledges support from a Discovery Grant awarded to Professor Joe Monaghan. J. Duarte and W. Schellart were supported by a Discovery Grant and Future Fellowship from the Australian Research Council awarded to Schellart. J. Duarte acknowledges the support by a DECRA grant from the Australian Research Council. The experiments were carried out in the Geodynamic Laboratory of the School of Geosciences at Monash University. CM dedicates this work to her parents who have made the elaboration of this manuscript possible. All the authors wish to thank the editor, John Brodholt, an anonymous reviewer, Kelsey Druken, and Changyeol Lee for their constructive comments, which improved the quality of the manuscript.

References

Atwater, T. (1970). Implications of plate tectonics for the Cenozoic tectonic evolution of western North America. Geological Society of America Bulletin, 81(12), 3513-3536.

Betts, P.G., D. Giles, J. Foden, B.F. Schaefer, G. Mark, G., M.J. Pankhurst, C.J. Forbes, H.A. Williams, N.C. Chalmers, N.C., and Q. Hills, Q. (2009), Mesoproterozoic plume-modified orogenesis in eastern Precambrian Australia, Tectonics 28, TC3006, doi:10.1029/2008TC002325.

Betts, P.G., W.G. Mason and L. Moresi (2012), The influence of a mantle plume head on the dynamics of a retreating subduction zone, Geology 40, 739-742.

Betts, P. G., Moresi, L., Miller, M. S., and Willis, D. (2015), Geodynamics of oceanic plateau and plume head accretion and their role in Phanerozoic orogenic systems of China, Geoscience Frontiers, 6(1), 49-59.

Chaytor, J. D., Keller, R. A., Duncan, R. A., and Dziak, R. P. (2007). Seamount morphology in the Bowie and Cobb hot spot trails, Gulf of Alaska. Geochem., Geophys., Geosyst, 8(9), doi: 10.1029/2007GC001712.

Clouard, V., and Bonneville, A. (2005). Ages of seamounts, islands, and plateaus on the Pacific plate. GSA Special Paper 388, 1-20.

Courtillot, V., Davaille, A., Besse, J., and Stock, J. (2003). Three distinct types of hotspots in the Earth's mantle. Earth Planet. Sci. Lett., 205(3), 295-308.

561 Dalziel, I.W.D., L.A. Lawer and J.B. Murphy (2000), Plumes, orogenesis and
562 supercontinental fragmentation, Earth Planet. Sci. Lett. 178, 1-11.

563 Davies, G.F. (1988) Ocean bathymetry and mantle convection; 1. large-
564 scale flow and hotspots. J. Geophys. Res. 93, 10467-10480, doi:
565 10.1029/JB093iB09p10467.

566 Druken, K.A., C. Kincaid, R.W. Griffiths, D.R. Stegman, and S.R. Hart
567 (2014), Plume-slab interaction: the Samoa-Tonga system, Phys. Earth
568 Planet. Int. 232, 1-14.

569 Fletcher, M., and Wyman, D. A. (2015). Mantle plume-subduction
570 zone interactions over the past 60 Ma, Lithos, 233, 162-173,
571 doi:10.1016/j.lithos.2015.06.026.

572 Geist, D., and M. Richards (1993), Origin of the Columbia Plateau and Snake
573 River plain: Deflection of the Yellowstone plume, Geology 21, 789-792.

574 Gorbatov, A., Y. Fukao, S. Widiyantoro, and E. Gordeev (2001), Seismic
575 evidence for a mantle plume oceanwards of the Kamchatka-Aleutian trench
576 junction, Geophys. J. Int. 146(2), 282-288.

577 Heron, P. J., J.P. Lowman, and C. Stein (2015). Influences on the positioning
578 of mantle plumes following supercontinent formation. J. Geophys. Res.
579 120(5), 3628-3648, doi:10.1002/2014JB011727.

580 Heuret, A. and Lallemand, S., 2005. Plate motions, slab dynamics
581 and back-arc deformation. Phys. Earth Planet. Int., 149(1), 31-51,
582 doi:10.1016/j.pepi.2004.08.022.

583 Kerr, R.C. and C. Mériaux (2004), Structure and dynamics of
584 sheared mantle plumes, Geochem. Geophys. Geosyst. 5, Q12009,
585 doi:10.1029/2004GC000749.

586 Kincaid, C., Ito, G., and Gable, C. (1995). Laboratory investigation of
587 the interaction of off-axis mantle plumes and spreading centres. Nature,
588 376(6543), 758-761.

589 Kincaid, C. and Griffiths, R.W., 2003. Laboratory models of the thermal
590 evolution of the mantle during rollback subduction. Nature, 425(6953),
591 58-62.

592 Kincaid, C., K.A. Druken, R.W. Griffiths, and D.R. Stegman (2013), Bi-
593 furcation of the Yellowstone plume driven by subduction-induced mantle
594 flow, Nature Geoscience 6, 395-399.

595 Lee, C., and Lim, C. (2014). Short-term and localized plume-slab interaction
596 explains the genesis of Abukuma adakite in Northeastern Japan. Earth
597 Planet. Sci. Lett., 396, 116-124.

598 Li, Z.-H., and N. M. Ribe (2012), Dynamics of free subduction from
599 3-D boundary element modeling, J. Geophys. Res. 117, B06408,
600 doi:10.1029/2012JB009165.

601 Mériaux, C.A. , J. C. Duarte, S. S. Duarte, W. P. Schellart, Z. Chen, F.
602 Rosas, J. Mata, and P. Terrinha (2015), Capture of the Canary mantle
603 plume material by the Gibraltar arc mantle wedge during slab rollback,
604 Geophys. J. Int. 201, 1717-1721.

Mériaux, C. A., Duarte, J. C., Schellart, W. P., and Mériaux, A. S. (2015). A two-way interaction between the Hainan plume and the Manila subduction zone. Geophys. Res. Lett. 42(14), 5796-5802, doi:10.1002/2015GL064313.

Montelli, R., Nolet, G., Dahlen, F. A., and Masters, G. (2006). A catalogue of deep mantle plumes: New results from finite-frequency tomography. Geochemistry, Geophysics, Geosystems, 7(11), doi: 10.1029/2006GC001248.

Morishige, M., Honda, S., and Yoshida, M. (2010). Possibility of hot anomaly in the sub-slab mantle as an origin of low seismic velocity anomaly under the subducting Pacific plate. Phys. Earth Planet. Int., 183(1), 353-365.

Murphy, J.B., G.L. Oppliger, and G.H. Brimhall (1998), Plume-modified orogeny: An example from the western United States, Geology 26, 731-734,

Obrebski, M., R.A. Allen, M. Xue, and S. Hung (2010), Slab-plume interaction beneath the Pacific Northwest, Geophys. Res. Lett. 37, L14305, doi:10.1029/2010GL043489.

Pesicek, J. D., Engdahl, E. R., Thurber, C. H., DeShon, H. R., and Lange, D. (2012). Mantle subducting slab structure in the region of the 2010 M8. 8 Maule earthquake (3040 S), Chile. Geophys. J. Int., 191(1), 317-324.

Ribe, N. M. (2010), Bending mechanics and mode selection in free subduction: A thin-sheet analysis. Geophys. J. Int., 180(2), 559-576.

Royden, L. H., and Husson, L. (2006). Trench motion, slab geometry and viscous stresses in subduction systems. Geophys. J. Int., 167(2), 881-905.

627 Russo, R. M., and Silver, P. G. (1994). Trench-parallel flow beneath the
628 Nazca plate from seismic anisotropy. Science, 263(5150), 1105-1111.

629 Schellart, W. P., Stegman, D. R., and Freeman, J. (2008). Global trench mi-
630 gration velocities and slab migration induced upper mantle volume fluxes:
631 Constraints to find an Earth reference frame based on minimizing viscous
632 dissipation. Earth-Science Rev., 88(1), 118-144.

633 Schellart, W., D. Stegman, R. Farrington and L. Moresi, L. (2011), Influence
634 of lateral slab edge distance on plate velocity, trench velocity, and subduc-
635 tion partitioning, J. Geophys. Res. 116, 1-15, doi: 10.1029/2011JB008535.

636 Schubert, G., D.L. Turcotte and P. Olson (2001), Mantle Convection in the
637 Earth and Planets, Cambridge University Press.

638 Sleep, N. H. (1990), Hotspots and mantle plumes: Some phenomenology, J.
639 Geophys. Res. 95, 6715-6736.

640 Smith, G. P., D. A. Wiens, K. M. Fischer, L. M. Dorman, S. C. Webb, and
641 J. A. Hildebrand, (2001), A complex pattern of mantle flow in the Lau
642 backarc, Science 292(5517), 713-716.

643 Smith, R. B., M. Jordan, B. Steinberger, C.M. Puskas, J. Farrell, G.P. Waite,
644 S. Husen, W.L. Chang, and R. OConnell (2009) Geodynamics of the Yel-
645 lowstone hotspot and mantle plume: Seismic and GPS imaging, kinemat-
646 ics, and mantle flow, J. Volcanol. Geotherm. Res. 188, 26-56.

647 Söderlund, U., S.A. Elming, R.E. Ernst, and D. Schissel (2006), The Cen-
648 tral Scandinavian Dolerite GroupProtracted hotspot activity or back-arc

649 magmatism?: Constraints from UPb baddeleyite geochronology and Hf
650 isotopic data, Precamb. Res. 150(3), 136-152.

651 Strak, V. and Schellart, W.P., 2014. Evolution of 3-D subduction-induced
652 mantle flow around lateral slab edges in analogue models of free subduc-
653 tion analysed by stereoscopic particle image velocimetry technique. Earth
654 Planet. Sci. Lett. 403, 368-379.

655 Thorkelson, D. J., Madsen, J. K., and Sluggett, C. L. (2011). Mantle flow
656 through the Northern Cordilleran slab window revealed by volcanic geo-
657 chemistry. Geology, 39(3), 267-270.

658 Von Huene, R., Miller, J.J. and Weinrebe, W., 2012. Subducting plate ge-
659 ology in three great earthquake ruptures of the western Alaska margin,
660 Kodiak to Unimak. Geosphere, 8(3), 628-644.

661 Weinstein, S.A. and Olson, P.L., 1989. The proximity of hotspots to conver-
662 gent and divergent plate boundaries. Geophys. Res. Lett., 16(5), 433-436.

663 Wyman, D.A., R. Kerrich, and D.I. Groves (1999), Lode Gold deposits
664 and Archean Mantle Plume-Island Arc interaction, Abitibi Subprovince,
665 Canada, J. Geology 107, 715-725.

666 Wyman, D.A., R. Kerrich, and A. Polat (2002), Assembly of Archean cra-
667 tonic mantle lithosphere and crust: plume-arc interaction in the Abibiti-
668 Wawa subduction-accretion complex, Precamb. Res. 115, 37-62.

669 Yáñez, G. A., Ranero, C. R., Huene, R., and Daz, J. (2001). Magnetic
670 anomaly interpretation across the southern central Andes (3234 S): The

role of the Juan Fernndez Ridge in the late Tertiary evolution of the margin. J. Geophys. Res. 106(B4), 6325-6345.

Zhao, D. (2007). Seismic images under 60 hotspots: search for mantle plumes, Gondwana Research, 12(4), 335-355.

S1. Appendix Supplementary Material: Slab/Plume system

S1.1. Model parameters

	Variable	Units
Ambient Fluid		
Gravitational acceleration	g	m s^{-2}
Ambient fluid density	ρ_a	kg m^{-3}
Ambient fluid viscosity	μ_a	Pa s
Ambient fluid depth	H	m
Plate		
Plate density	ρ_s	kg m^{-3}
Plate density contrast	$\Delta\rho_s = \rho_s - \rho_a$	kg m^{-3}
Plate viscosity	μ_s	Pa s
Plate length	L	cm
Plate width	W	cm
Plate thickness	d	cm
Slab length	l	cm
Plate velocity	U	cm s^{-1}
Plume		
Plume density	ρ_p	kg m^{-3}
Plume density contrast	$\Delta\rho_p = \rho_a - \rho_p$	kg m^{-3}
Plume viscosity	μ_p	Pa s
Plume volume flux	Q	m^3 s^{-1}
Plume buoyancy flux	$B_p/g = \Delta\rho_p Q$	kg s^{-1}
Initial Variables		
Slab initial bending lengths	$l(0),\ l_b(0)$	cm
Initial dip angle of the slab	θ_0	degrees
Time of plume initiation	t_p^i	s
Plume source position relative to slab	F, R, S	

Table S1.1: Experimental variables. F, R, and S refer to Front, Rear and Side initial plume position relative to the slab, respectively.

S1.2. Dimensional analysis

Discarding the initial variables, the system depends on the 11 following primary variables: g, μ_a, H, $\Delta\rho_s$, μ_s, U, W, d, l, μ_p, and $B_p/g = \Delta\rho_p Q$, and has three fundamental dimensions (mass, length and time). We note that the dynamics of subduction has been shown not to depend on the length of the plate L (Li and Ribe, 2012). Consequently, according to the Buckingham Π theorem, the system depends on 8 dimensionless numbers. Dimensional analysis then yields

$$\mathcal{F}\left(\frac{gd}{U^2}, \frac{\mu_a}{\Delta\rho_s U d}, \frac{H}{d}, \frac{\mu_s}{\Delta\rho_s U d}, \frac{W}{d}, \frac{l}{d}, \frac{\mu_p}{\Delta\rho_s U d}, \frac{B_p/g}{\Delta\rho_s U d^2}\right) = 0, \tag{1}$$

which we can rewrite

$$\mathcal{G}\left(\frac{U^2}{gd}, \frac{\Delta\rho_s U d}{\mu_a}, \frac{H}{d}, \frac{\mu_s}{\mu_a}, \frac{W}{d}, \frac{l}{d}, \frac{\mu_p}{\mu_a}, \frac{\Delta\rho_s U d W}{B_p/g}\right) = 0, \tag{2}$$

or

$$\mathcal{G}\left(Fr, Re, \frac{\mu_s}{\mu_a}, \frac{\mu_p}{\mu_a}, \frac{H}{d}, \frac{W}{d}, \frac{l}{d}, \frac{B_s}{B_p}\right) = 0, \tag{3}$$

using the definition of the slab buoyancy flux $B_s/g = \Delta\rho_s U W d$, and identifying that the two first dimensionless groups in equation 2 are the Froude number and Reynolds number, respectively. Equation 3 points out that one important dimensionless number of the problem is the slab/plume buoyancy flux ratio. Now, physical considerations point out that the system could also depend on the initial position tip of the slab, and hence the stiffness of the plate S (see Suppl. Inf. S2 for further details), the time of plume initiation, and the plume relative to the slab, for which a formal variable cannot simply be defined. We will show that the subduction dynamics ultimately does not depend on the tip initial conditions whereas the plume initial conditions will impact on the nature of the interaction.

S2. Appendix. Supplementary Material: Experimental Analyses

S2.1. Extent of the slab-induced poloidal and toroidal cell at the surface

Experiment	γ	l	r_F	r_R
3 (Slab-only)	836	8 cm (40 km)	33 cm (1650 km)	2 cm (100 km)
		16 cm (800 km)	48 cm (2400 km)	10 cm (500 km)
		32 cm (1600 km)	62 cm (3100 km)	19 cm (950 km)
4	610	8 cm (40 km)	43 cm (2150 km)	<2.5 cm (<125 km)
		16 cm (800 km)	52 cm (2600 cm)	10 cm (500 km)
		32 cm (1600 km)	68 cm (3400 cm)	16 cm (800 km)
12	538	8 cm (40 km)	34 cm (1700 km)	<2 cm (<100 km)
		16 cm (800 km)	40 cm (2000 km)	12 cm (600 km)
		32 cm (1600 km)	61 cm (3050 km)	19 cm (950 km)

Table S2.1: Extent of the slab-induced poloidal and toroidal flow seen at the surface as a function of slab length for three experiments. The distances r_F & r_R are estimated at the surface as the distances from the trench in the front and rear regions of the slab, where the slab-induced poloidal inflow (front region) and toroidal outflow (rear region) respectively vanishes.

Those distances r_F & r_R are estimates only as they are inferred from the displacement of the neutrally buoyant tracers that had been seeded at the surface, but they give a good indication of where plumes can be influenced by the slab once arrived at the surface. Regardless of the slab length, front plumes will likely be caught in the poloidal flow from thousands of kilometres away from the trench, whereas rear plumes will not be affected by the toroidal flow unless they are close to the trench or the slab is long.

S2.2. Initial tip length l, Bending length l_b, Stiffness S_0 and sinking regimes

As the plate was systematically bent initially from a length $l_{top} = 3$ cm measured from above as shown in Figure S2.1a, the initial tip length $l(0)$ was calculated as

$$l(0) = \frac{l_{top}}{\cos(\theta_0)}, \tag{1}$$

where θ_0 was the initial angle the slab made with the surface as shown in Figure S2.1b. As l_{top} and θ_0 were measured within a maximum error of 0.2 cm and 3 degrees, respectively, $l(0)$ was estimated within a typical error of 7%.

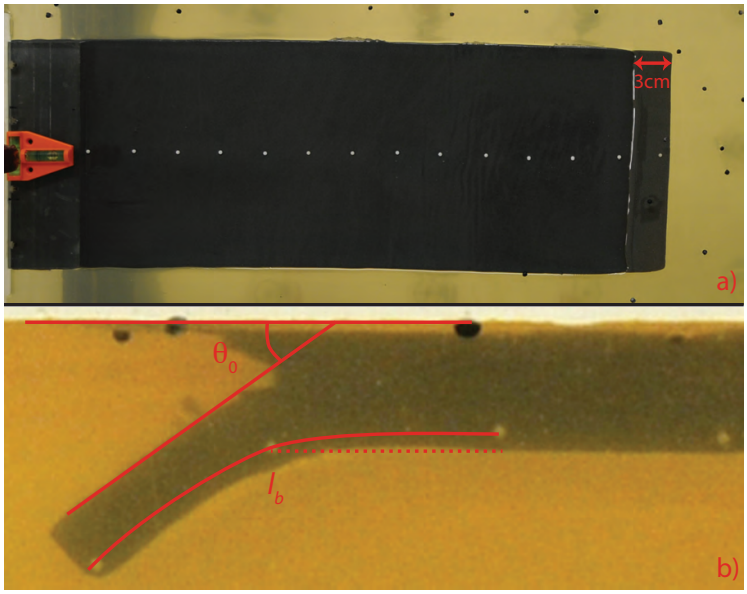

Figure S2.1: a) Initial slab tip seen from above. b) Close-up of Initial slab tip seen from the side showing the initial dip angle of the slab θ_0, and the length of curvature $l_b(0)$. Note that the distance between the white markers was 4 cm.

The initial bending length $l_b(0)$ was measured to within 5% from the photos of the side-view as shown in Figure S2.1b. For experiments 3 & 13-18,

however, the initial plate curvature could not be seen. We attribute this to an initial smaller curvature, equivalently larger radius of curvature and hence larger initial bending length $l_b(0)$ of these latter experiments compared to the other experiments, which can be explained by their larger γ ratio (up to a factor 1.6) (Schellart, 2010; Capitanio and Morra, 2012).

The initial plate stiffness S_0, defined by

$$S_0 = \gamma \left(\frac{d}{l_b(0)} \right)^3 \tag{2}$$

was then estimated for experiments 1-2, 4-12 & 19-21, for which $l_b(0)$ could be estimated. Values of S_0 are greater than 3, which suggests that the observed sinking regime would initially not be in a Stokes dominated regime but rather in the transition between a Stokes dominated regime and a stiffness dominated regime (Ribe, 2010; Li and Ribe, 2012). Consequently, for experiments 3 & 13-18, it cannot be excluded that the larger values of $l_b(0)$ resulted in a smaller value of $S_0 \lessapprox 3$, and hence, compared with experiments 1-2, 4-12 & 19-21, may have not initially been as dependent on the bending. Yet as sinking proceeds, the slab length l and and the slab bending length l_b increase with time. The plate stiffness defined by $S = \gamma(d/l)^3$ is thus to decrease with time and the steady sinking rate is consequently expected to settle in the Stokes regime, in which U varies as μ_a^{-1} (Li and Ribe, 2012).

735 *S2.3. Profiles of the tip vertical position as a function of time for experiments*
736 *at buoyancy ratio* ≈ 15

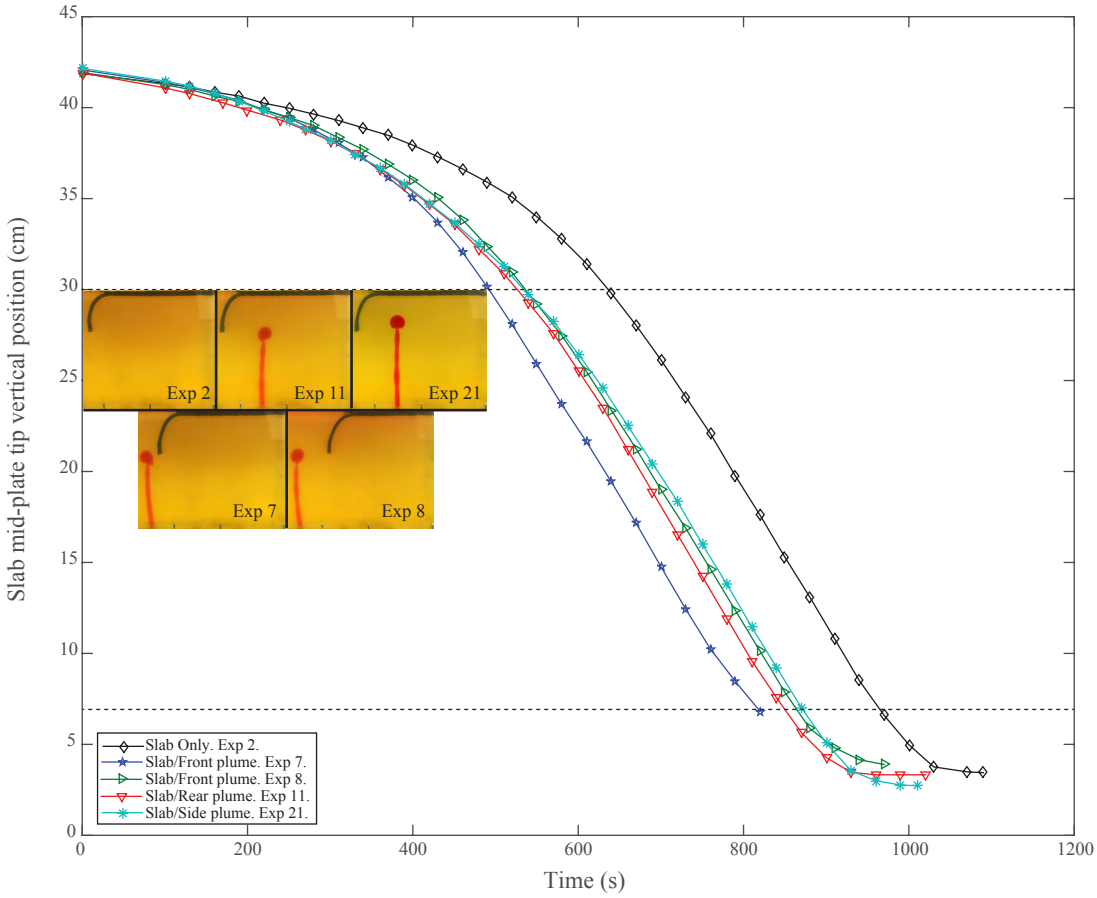

Figure S2.2: Slab tip vertical positions as a function of time for the slab only experiment 2 and, slab and Front, Rear and Side plume experiments 7, 8, 11 & 21, respectively. The two dashed lines indicate the two vertical positions between which linear regressions on the slab tip positions were made to determine the slab steady sinking rates U given in Table 1. The five inserts show the slab and plume positions when the slab tip is at the vertical position of 30 cm from where the linear regressions start.

S2.4. Estimates of F_b and F_p.

Experiment	$l(t_p^s)$ (m)	$A(t_p^s)$ (m^2)	F_p (kg m s^{-2})	F_b (kg m s^{-2})	F_p/F_b %
14	0.04	0.0408	0.0135	0.0471	29
15	0.12	0.0276	0.0311	0.1413	22
18	0.08	0.0554	0.0200	0.0942	21

Table S2.2: Vertical forces F_b and F_p at the time t_p^s of plume spreading initiation underneath the plate.

S2.5. Plume tilts

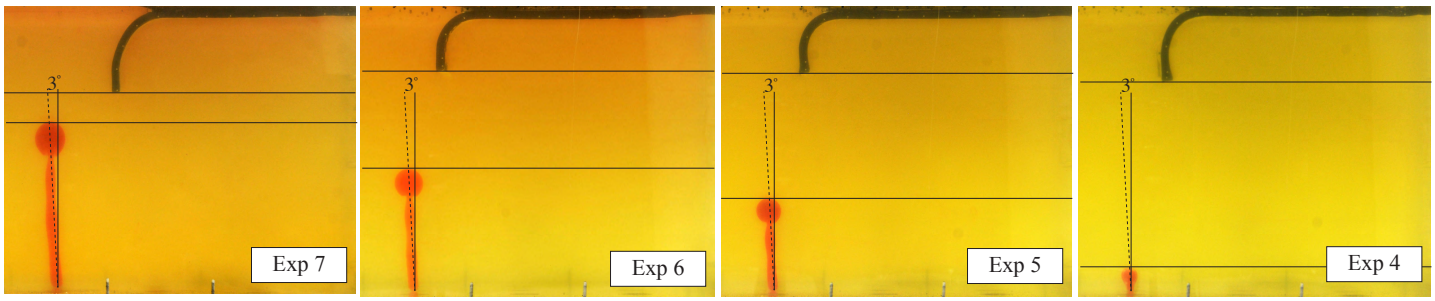

Figure S2.3: Snapshots of slab/plume positioning for experiments 4, 5, 6 & 7, from bottom to top, at the time the plume is tilted by three degrees to the vertical.

During its ascent, a plume responds to the ambient shear, and assuming horizontal shear, the angle α of tilt in the direction of shear from the vertical at some depths follows a simple relationship between the shear velocity U_s at that depth, and the plume Stokes velocity U_p (Richards and Griffiths, 1988)

$$\tan \alpha \approx \frac{U_s}{2U_p}, \tag{3}$$

743 which can be related to the plume buoyancy B_p (Kerr & Mériaux, 2004)
744 leading to

$$\tan \alpha \approx \frac{U_s}{2} \frac{\sqrt{\mu_a/\mu_p}}{k\sqrt{8B_p/\pi\mu_a}}, \tag{4}$$

745 where k for compositional plumes has a value of 0.54 (Richards and Grif-
746 fiths, 1988). According to equation 4, a shear 2-3 times larger was necessary
747 to achieve the same tilt on the plume between experiments 4 and 7, or equiv-
748 alently the ambient slab-induced shear velocity U_s increases with height by
749 at least a factor 2-3. The shear rate estimates represented 1.4 to 3% of the
750 sinking rates between experiments 4 and 7.

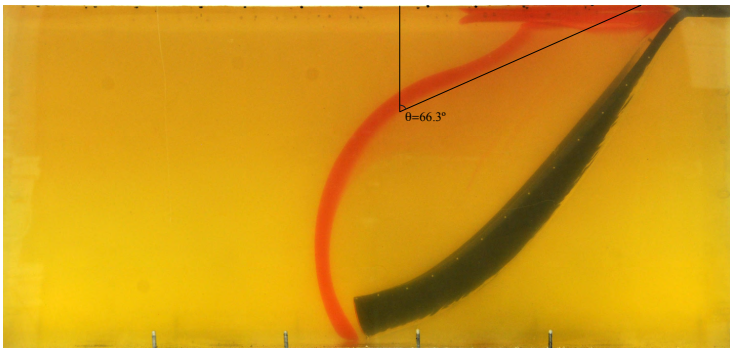

Figure S2.4: Maximum tilt of 66.3^o encountered in the first 14 cm (700 km) from the surface in experiment 8.

S2.6. Sensitivity of slab/plume relative position

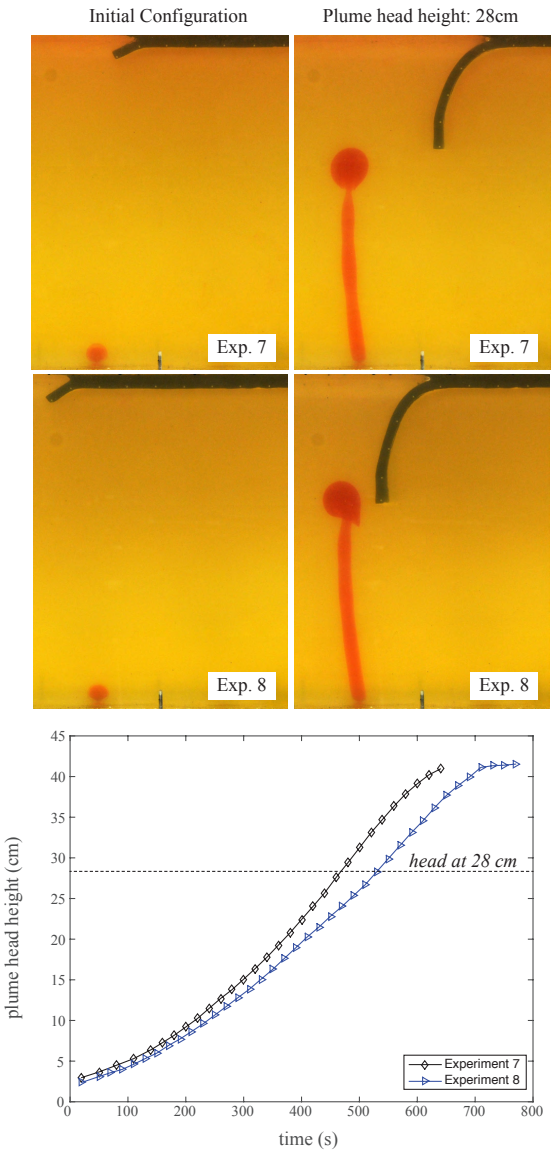

Figure S2.5: Experiments 7 & 8 of similar B_s/B_p: 1) Plume and slab initial configuration (top left photos), 2) Plume and slab configuration shown when the plume head is at 28 cm (top right photos), and 3) Plume head vertical height as a function of time.

S3. Appendix. Supplementary Material: Application to Nature.

S3.1. Range of slab/plume buoyancy flux ratios B_s/B_p in nature.

Nature	W (km)	d (km)	$\Delta\rho_s$ (kg/m^3)	U (cm/yr)	B_s/g $\times 10^5$(kg/s)	B_p/g (kg/s)	B_s/B_p
Fast & Very wide subduction zone/Weakest plume	7000	75	80	10	1.42	200	710
Fast & Very wide subduction zone/Medium plume	7000	75	80	10	1.42	1000	355
Fast & Very wide subduction zone/Strongest plume	7000	75	80	10	1.42	6400	142
Fast & Wide subduction zone/Weakest plume	1000	75	80	10	0.71	200	101
Fast & Wide subduction zone/Medium plume	1000	75	80	10	0.71	1000	51
Fast & Wide subduction zone/Strongest plume	1000	75	80	10	0.71	6400	20
Fast & Narrow subduction zone/Weakest plume	400	75	80	10	0.28	200	40
Fast & Narrow subduction zone/Medium plume	400	75	80	10	0.28	1000	20
Fast & Narrow subduction zone/Strongest plume	400	75	80	10	0.28	6400	8
Medium speed & Very wide subduction zone/Weakest plume	7000	75	80	5	0.20	200	142
Medium speed & Very wide subduction zone/Medium plume	7000	75	80	5	0.20	1000	71
Medium speed & Very wide subduction zone/Strongest plume	7000	75	80	5	0.20	6400	28
Medium speed & Wide subduction zone/Weakest plume	1000	75	80	5	0.10	200	20
Medium speed & Wide subduction zone/Medium plume	1000	75	80	5	0.20	1000	10
Medium speed & Wide subduction zone/Strongest plume	1000	75	80	5	0.20	6400	4
Medium speed & Narrow subduction zone/Weakest plume	400	75	80	5	0.04	200	8
Medium speed & Narrow subduction zone/Medium plume	400	75	80	5	0.04	1000	4
Medium speed & Narrow subduction zone/Strongest plume	400	75	80	5	0.04	6400	1.6
Slow & Very wide subduction zone/Weakest plume	7000	75	80	2	0.08	200	22
Slow & Very wide subduction zone/Medium plume	7000	75	80	2	0.08	1000	11
Slow & Very wide subduction zone/Strongest plume	7000	75	80	2	0.08	6400	4.4
Slow & Wide subduction zone/Weakest plume	1000	75	80	2	0.04	200	3.2
Slow & Wide subduction zone/Medium plume	1000	75	80	2	0.04	1000	1.6
Slow & Wide subduction zone/Strongest plume	1000	75	80	2	0.04	6400	0.6
Slow & Narrow subduction zone/Weakest plume	400	75	80	2	0.0162	200	1.3
Slow & Narrow subduction zone/Medium plume	400	75	80	2	0.0162	1000	0.6
Slow & Narrow subduction zone/Strongest plume	400	75	80	2	0.0162	6400	0.2

Table S3.1: Natural range of slab/plume buoyancy flux ratios on the basis of modern range of slab width, slab velocity and plume buoyancy. We have assumed constant values of d and $\Delta\rho_s$, which can vary but to a lesser degree. The buoyancy flux B_p for a medium plume is based on a statistical analysis (Mériaux et al., 2015b; Supplementary Information). The range of possible buoyancy flux ratios is 0.2–710.

S3.2. Some modern plumes in the vicinity of a trench.

S3.2.1. The Cascadia/Bowie and Cobb systems

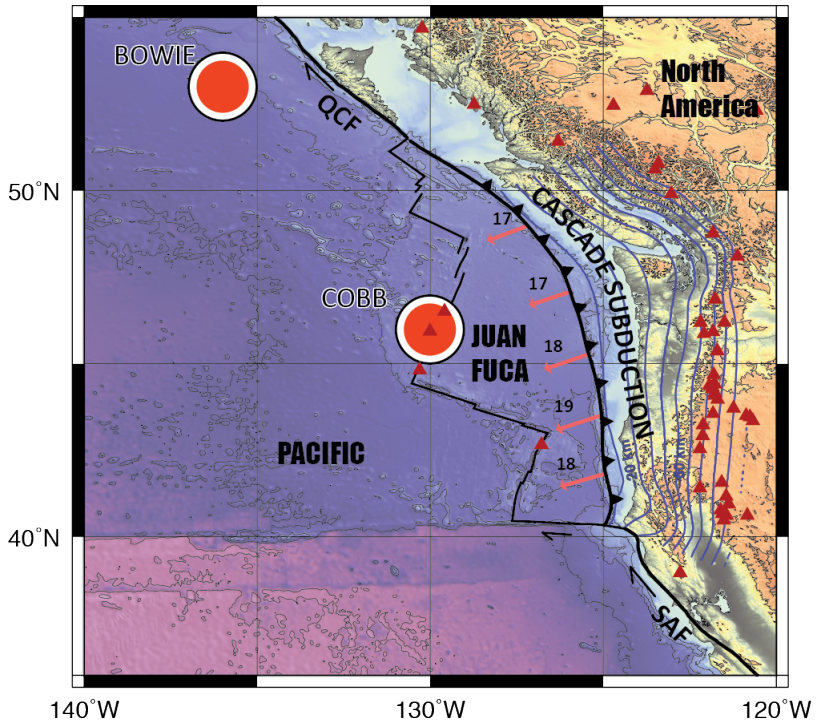

Figure S3.1: Bowie and Cobb hotspots in the vicinity of the Cascadia subduction zone. Topography and bathymetry with black contours every 1 km are from ETOPO1 [Amante and Eakins, 2009] . The red triangles are active volcanoes and the red arrows show the rollback of the cascade trench. Absolute velocities of the trench motions (in mm/yr) are calculated in the GSRM-APM-1 hotspot reference frame (Kreemer, 2009). Plate boundaries are modified from Bird (2003). SAF: San Andreas Fault, QCF: Queen Charlotte Fault. The slab surface is highlighted by blue contours at 10 km intervals (Hayes et al., 2012).

An additional movie named PlateKinematic-HS-since60Ma.m4v is provided to show the plate reconstruction over the Bowie, Cobb and Yellowstone plumes in the last 60 Ma, assuming that the three hotspots are as old. The conditions for slab/rear plume interactions might have only been met between 40-60 Ma for Bowie, and 45-60 Ma for Cobb, and involve the two subduction zones of Alaska and British Columbia where the Kula plate subducted under North America (NA). Yet, at the time, plumes being located at least 900 km away from the nearest trench, only the slab-induced poloidal flow may have played a role in capturing the rear plume material towards the trench. Note the evolution of the Juan de Fuca subduction zone width over the last 30 Ma and the activation of the Queen Charlotte and San Andreas strike-slip faults, north and south respectively of the Juan Fuca plate. The evolution of the Juan Fuca plate subduction also affected its interaction with the 16 Ma Yellowstone front plume. Overall, the complex geodynamic history of the region has likely resulted in some atypical spreading of plume material, which should encourage further geochemical/petrological and/or seismological investigations. All the plate reconstructions were made using GPlates 1.5 (www.gplates.org) using the plate boundaries and kinematics of Zahirovic et al. (2015).

S3.2.2. The Nazca/San Felix and Juan Fernández systems

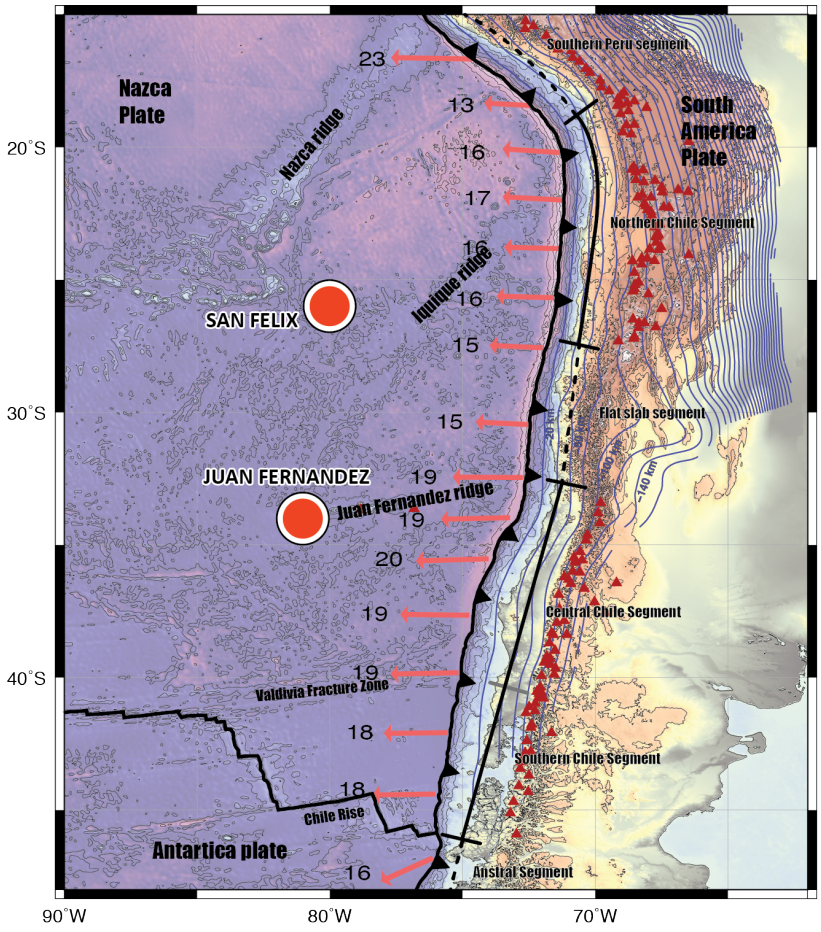

Figure S3.2: San Felix and Juan Fernández hotspots at the rear of two retreating segments of the South-American subduction zone. Topography and bathymetry with black contours every 1 km are from ETOPO1 [Amante and Eakins, 2009]. The red triangles are active volcanoes and the red arrows show the rollback of the Peru-Chile trench. Absolute velocities of the trench motions (in mm/yr) are calculated in the GSRM-APM-1 hotspot reference frame (Kreemer, 2009). Plate boundaries are from Bird (2003). The slab surface is highlighted by blue contours at 20 km intervals (Hayes et al., 2012). The two northern and southern shorter slab segments are indicated with the tick mark delimited black lines.

Slab/Plume systems	Time	Mean Slab depth	Trench mode	Plume/Trench Position	R_{pt}	B_p/g	d	$U^{(a)}$	U_t $^{(a)}$	W	B_s/g	B_s/B_p
	Ma.	km			km	kg/s	km	cm/yr	cm/yr	km	kg/s	
This study												
Cascadia/Bowie	0	1200	Retreating	Rear/Side	320	600	35	2.2	1.8	1400	2,735	5
Cascadia/Cobb	0	1200	Retreating	Rear	330	300	35	2.2	1.8	1400	2,735	9
Nazca/San Felix	0	600	Quasi stationary	Rear	820	1600-2300	80	2.7	0.7	6000	32,877	14-20
								3.5	0.5	910	6,464	3-4
Nazca/Juan Fernandéz	0	140	Quasi stationary	Rear	835	1600-1700	80	2.7	0.7	6000	73,059	14-20
								3.8	1.6	2940	22,673	10-14
Java/South Java$^{(b)}$	0	1000	Retreating	Rear	150	1000	105	3.8	1.8	1700	17,207	17
San Cristobal/East of Solomon$^{(b)}$	0	500	Stationary	Front	700	1000	68	2.8	0.0	1450	7,000	7
New Hebrides/Coral Sea$^{(b)}$	0	400	Retreating	Rear	1200	1000	85	5.2	6.6	1300	14,576	14
Previous studies												
Manila/Hainan	0	670	Retreating	Rear	1000	1000	65	3.1	2.3	5,112	10	5
Gibraltar/Canary	-10	660	Retreating	Side	150	290-570	75	2.5	2.0	400	1900	3-7
Tonga/Samoa	0	1000	Retreating	Rear/Side	700	1600	120	6.8	6.8	3400	70,380	44
Cascadia/Yellowstone	0	1200	Retreating	Front	1200	1500	35	2.2	1.8	1400	2735	2
	-15	?	Retreating	Front	380	1500	44	2.6	2.3	2000	5,804	4

Table S3.2: Some plumes in the vicinity of a slab. $^{(a)}$ We note that modes and velocities may vary between the different absolute reference frames, (1) hotspot reference frame of Gripp and Gordon (2002), which analyses the Pacific hotspot track; (2) hotspot reference frame of Gordon and Jurdy (1986), which considers both the Indo-Atlantic and the Pacific hotspot tracks; (3) hotspot reference frame of Steinberger et al. (2004), which investigates only the Indo-Pacific hotspot tracks; (4) no-net-rotation reference frame (Gripp and Gordon, 2002), and (5) a subduction zone reference frame (Schellart, 2011). Here we have adopted subduction modes and subduction velocities of Schellart et al. (2011), and Schellart et al. (2010). $^{(b)}$ refers to lower mantle starting plumes. Today's slab depths were taken from Hayes et al. (2012), Fukao and Obayashi (2013), and Gutscher et al. (2002). R_{pt} is an estimate of the distance between the trench and the plume. For B_p, we used values from Davies (1988), Sleep (1990), Steinberger (2000), and Courtillot et al. (2003). When not available, we used the buoyancy flux of 1000 kg/s for a medium plume based on a statistical analysis (Mériaux et al., 2015b; Supplementary Information). d was estimated from plate ages (Heuret and Lallemand, 2005) according to d (km) $\sim 7+11\times\sqrt{(}age$ (Ma). The sinking rate U was calculated from the along-trench averaged subduction rate assuming a slab dip angle of 45 degrees. U_t is the retreat rate. We have used the slab widths W of Schellart et al. (2007) given in the Supplementary Information and measured those which Schellart et al. (2007) did not provide. A value $\Delta\rho_s$ of 80 kg/m^3 was used to calculate B_s/g.

S3.3. Slab/plume systems from magmatism

Slab/Plume system	Age	Volcanism	Reference
Abitibi- Wawa arc/plume	$\sim$ 2700 Ma	southern Superior Province	Wyman et al. (2002)
Baltic arc/plume	$\sim$ 2700 Ma	Sumozero-Kenozero greenstone belt	Puchtel et al. (1999)
Paleo-Pacific arc/Karoo plume	270 Ma	Patagonia calc-alkaline arc magmatism	Rapela et al. (2005)
East Asia Pacific arc/plume	140 Ma	Adakitic arc	Lee and Ryu (2015)
Izu-Bonin-Mariana arc/Oki-Daito plume	50 Ma	Oceanic plateaus on the Philippine Sea plate	Ishizuka et al. (2013)
		Benham Plateau	Deschamps and Lallemand (2003)
		Manus Basin	Macpherson and Hall (2001)
Cocos arc/Baja-Guadalupe plume (??)	10 Ma	Mexican volcanic belt	Márquez et al. (1999)
Ionian arc/Etna plume	0 Ma	Mount Etna	Schiano et al. (2001)
Tonga arc/Samoa plume	14-0 Ma	Volcanoes of Tafahi and Niuatoputapu, and Lau basin	Ewart et al. (1998)
Cascadia arc/Yellowstone plume	17.5-0 Ma	Columbia plateau	Geist and Richards (1993)

Table S3.3: Slab/plume systems where mixed plume and arc magmatism have been reported. This list is not exhaustive.

References

Amante, C. and B. W. Eakins (2009), ETOPO1 1 arc-minute global relief model: Procedures, data sources and analysis, NOAA Technical Memorandum NESDIS NGDC-24, Natl. Geophys. Data Cent., doi:10.7289/V5C8276M.

Bird, P. (2003), An updated digital model of plate boundaries, Geochem. Geophys. Geosyst., 4(3), 1027, doi:10.1029/2001GC000252.

Capitanio, F. A., and Morra, G. (2012). The bending mechanics in a dynamic subduction system: Constraints from numerical modelling and global compilation analysis. Tectonophysics, 522, 224-234, doi:10.1016/j.tecto.2011.12.003.

Courtillot, V., Davaille, A., Besse, J., and Stock, J. (2003). Three distinct types of hotspots in the Earth's mantle. Earth Planet. Sci. Lett., 205(3), 295-308.

Davies, G. F. (1988), Ocean bathymetry and mantle convection: 1. Large-scale flow and hotspots, J. Geophys. Res. 93, 10,467-10,480.

Deschamps, A. and Lallemand, S., 2003. Geodynamic setting of Izu-Bonin-Mariana boninites. Geological Society, London, Special Publications, 219(1), 163-185.

Ewart, A., Collerson, K. D., Regelous, M., Wendt, J. I., and Niu, Y. (1998). Geochemical evolution within the Tonga-Kermadec-Lau arc-back-arc systems: the role of varying mantle wedge composition in space and time. J. Petrol., 39(3), 331-368.

800 Fukao, Y., and M. Obayashi (2013), Subducted slabs stagnant above, pene-
801 trating through, and trapped below the 660 km discontinuity, J. Geophys.
802 Res. Solid Earth, 118, 59205938, doi:10.1002/2013JB010466.

803 Geist, D., and M. Richards (1993), Origin of the Columbia Plateau and Snake
804 River plain: Deflection of the Yellowstone plume, Geology 21, 789-792.

805 Gordon, R. G., and Jurdy, D. M. (1986). Cenozoic global plate motions. J.
806 Geophys. Res, 91(12), 389-12.

807 Gripp, A. E., and R. G. Gordon (2002), Young tracks of hotspots and cur-
808 rent plate velocities, Geophys. J. Int., 150, 321361, doi:10.1046/j.1365-
809 246X.2002.01627.x.

810 Gutscher, M.A., Malod, J., Rehault, J.P., Contrucci, I., Klingelhoefer, F.,
811 Mendes-Victor, L. and Spakman, W., 2002. Evidence for active subduction
812 beneath Gibraltar. Geology, 30(12), 1071-1074.

813 Hayes, G. P., D. J. Wald, and R. L. Johnson (2012), Slab1.0: A three-
814 dimensional model of global subduction zone geometries, J. Geophys. Res.,
815 117, B01302, doi:10.1029/2011JB008524.

816 Heuret, A. and Lallemand, S., 2005. Plate motions, slab dynamics and back-
817 arc deformation. Phys. Earth Planet. Int., 149(1), 31-51.

818 Ishizuka, O., Taylor, R.N., Ohara, Y. and Yuasa, M., 2013. Upwelling, rift-
819 ing, and age-progressive magmatism from the Oki-Daito mantle plume.
820 Geology, 41(9), 1011-1014.

821 Kerr, R.C. and C. Mériaux (2004), Structure and dynamics of
822 sheared mantle plumes, Geochem. Geophys. Geosyst. 5, Q12009,
823 doi:10.1029/2004GC000749.

824 Kreemer, C. (2009), Absolute plate motions constrained by shear wave split-
825 ting orientations with implications for hotspot motions and mantle flow,
826 J. Geophys. Res., 114, B10405, doi:10.1029/2009/JB006416.

827 Lee, C. and Ryu, I.C. (2015), A new tectonic model for the genesis of Adakitic
828 arc magmatism in Cretaceous East Asia. Subduction Dynamics: From
829 Mantle Flow to Mega Disasters, 211, 69-79.

830 Li, Z.-H., and N. M. Ribe (2012), Dynamics of free subduction from
831 3-D boundary element modeling, J. Geophys. Res. 117, B06408,
832 doi:10.1029/2012JB009165.

833 Macpherson, C.G. and Hall, R., 2001. Tectonic setting of Eocene boninite
834 magmatism in the IzuBoninMariana forearc. Earth and Planetary Science
835 Letters, 186(2), 215-230.

836 Márquez, A., Oyarzun, R., Doblas, M. and Verma, S.P., 1999. Alkalic (ocean-
837 island basalt type) and calc-alkalic volcanism in the Mexican volcanic belt:
838 A case for plume-related magmatism and propagating rifting at an active
839 margin?. Geology, 27(1), 51-54.

840 Mériaux, C. A., Duarte, J. C., Schellart, W. P., and Mériaux, A. S. (2015). A
841 two-way interaction between the Hainan plume and the Manila subduction
842 zone. Geophys. Res. Lett. 42(14), 5796-5802 , doi:10.1002/2015GL064313.

Puchtel, I.S., Hofmann, A.W., Amelin, Y.V., Garbe-Schnberg, C.D., Samsonov, A.V. and Shchipansky, A.A., 1999. Combined mantle plume-island arc model for the formation of the 2.9 Ga Sumozero-Kenozero greenstone belt, SE Baltic Shield: Isotope and trace element constraints. Geochimica et Cosmochimica Acta, 63(21), 3579-3595.

Rapela, C.W., Pankhurst, R.J., Fanning, C.M. and Herve, F., 2005. Pacific subduction coeval with the Karoo mantle plume: the Early Jurasssic Subcordilleran belt of northwestern Patagonia. Geological Society, London, Special Publications, 246(1), 217-239.

Ribe, N. M. (2010), Bending mechanics and mode selection in free subduction: A thin-sheet analysis. Geophys. J. Int., 180(2), 559-576.

Richards, M.A. and Griffiths, R.W., 1988. Deflection of plumes by mantle shear flow: experimental results and a simple theory. Geophys. J. 94(3), 367-376.

Schellart, W.P., Freeman, J., Stegman, D.R., Moresi, L. and May, D., 2007. Evolution and diversity of subduction zones controlled by slab width. Nature, 446(7133), 308-311.

Schellart, W. P. (2010). Evolution of subduction zone curvature and its dependence on the trench velocity and the slab to upper mantle viscosity ratio. J. Geophys. Res. 115, B11406, doi:10.1029/2009JB006643.

Schellart, W.P., Stegman, D.R., Farrington, R.J., Freeman, J. and Moresi, L. (2010). Cenozoic tectonics of western North America controlled by evolving width of Farallon slab. Science, 329(5989), 316-319.

866 Schellart, W. P. (2011), A subduction zone reference frame based on slab ge-
867 ometry and subduction partitioning of plate motion and trench migration,
868 Geophys. Res. Lett., 38, L16317, doi:10.1029/2011GL048197.

869 Schiano, P., Clocchiatti, R., Ottolini, L., and Busà, T. (2001). Transition of
870 Mount Etna lavas from a mantle-plume to an island-arc magmatic source.
871 Nature, 412(6850), 900-904.

872 Sleep, N. H. (1990), Hotspots and mantle plumes: Some phenomenology, J.
873 Geophys. Res. 95, 6715-6736.

874 Steinberger, B., 2000. Plumes in a convecting mantle: Models and observa-
875 tions for individual hotspots. J. Geophys. Res. 105(B5), 11127-11152.

876 Steinberger, B., R. Sutherland, and R. J. O' Connell (2004), Prediction of
877 Emperor-Hawaii seamount locations from a revised model of global motion
878 and mantle flow, Nature, 430, 167 -173, doi:10.1038/nature02660.

879 Wyman, D.A., R. Kerrich, and A. Polat (2002), Assembly of Archean cra-
880 tonic mantle lithosphere and crust: plume-arc interaction in the Abibiti-
881 Wawa subduction-accretion complex, Precamb. Res. 115, 37-62.

882 Zahirovic, S., Müller, R. D., Seton, M., and Flament, N. (2015). Tectonic
883 speed limits from plate kinematic reconstructions. Earth Planet. Sci. Lett.,
884 418(C), 40-52.